THESIS

QUANTITATIVE PRECIPITATION ESTIMATION FOR AN X-BAND WEATHER RADAR NETWORK

Submitted by

Haonan Chen

Department of Electrical and Computer Engineering

In partial fulfillment of the requirements

For the Degree of Master of Science

Colorado State University

Fort Collins, Colorado

Spring 2013

Committee Member:

Advisor: V. Chandrasekar

Branislav M. Notaros
Paul W. Mielke

ABSTRACT

QUANTITATIVE PRECIPITATION ESTIMATION FOR AN X-BAND WEATHER RADAR NETWORK

Currently, the Next Generation (NEXRAD) radar network, a joint effort of the U.S. Department of Commerce (DOC), Defense (DOD), and Transportation (DOT), provides radar data with updates every five-six minutes across the United States. This network consists of about 160 S-band (2.7 to 3.0 GHz) radar sites. At the maximum NEXRAD range of 230 km, the 0.5 degree radar beam is about 5.4 km above ground level (AGL) because of the effect of earth curvature. Consequently, much of the lower atmosphere (1-3 km AGL) cannot be observed by the NEXRAD. To overcome the fundamental coverage limitations of today's weather surveillance radars, and improve the spatial and temporal resolution issues, the National Science Foundation Engineering Center (NSF-ERC) for Collaborative Adaptive Sensing of the Atmosphere (CASA) was founded to revolutionize weather sensing in the lower atmosphere by deploying a dense network of shorter-range, low-power X-band dual-polarization radars. The distributed CASA radars are operating collaboratively to adapt the changing atmospheric conditions. Accomplishments and breakthroughs after five years operation have demonstrated the success of CASA program.

Accurate radar quantitative precipitation estimation (QPE) has been pursued since the beginning of weather radar. For certain disaster prevention applications such as flash flood and landslide forecasting, the rain rate must however be measured at a high spatial and temporal resolution. To this end, high-resolution radar QPE is one of the major research activities conducted by the CASA community. A radar specific differential propagation phase (Kdp)-based QPE methodology has been developed in CASA. Unlike the rainfall estimation based on the power terms such as radar reflectivity (Z) and differential reflectivity (Zdr), Kdp-based QPE is less sensitive to the path attenuation, drop size distribution (DSD), and radar calibration errors. The CASA Kdp-based QPE system is also immune to the partial beam blockage and hail contamination.

The performance of the CASA QPE system is validated and evaluated by using rain gauges. In CASA's Integrated Project 1 (IP1) test bed in Southwestern Oklahoma, a network of 20 rainfall gauges is used for

cross-comparison. 40 rainfall cases, including severe, multicellular thunderstorms, squall lines and widespread stratiform rain, that happened during years 2007 - 2011, are used for validation and evaluation purpose. The performance scores illustrate that the CASA QPE system is a great improvement compared to the current state-of-the-art.

In addition, the high-resolution CASA QPE products such as instantaneous rainfall rate map and hourly rainfall amount measurements can serve as a reliable input for various distributed hydrological models. The CASA QPE system can save lived and properties from hazardous flash floods by incorporating hydraulic and hydrologic models for flood monitoring and warning.

ACKNOWLEDGEMENTS

First and foremost, I want to express my deep appreciation to Dr. V. Chandrasekar. It has been a great honor to study and do research under the supervision of Dr. Chandra. This work would never have been accomplished without his invaluable guidance and encouragement. He is my mentor not only in research, but also in life.

I also sincerely thank Drs. Branislav M. Notaros and Paul W. Mielke for serving as my graduate committee members.

I highly appreciate assistance from my colleagues working in the Radar and Communications Group at Colorado State University and all the CSU-CHILL radar staff, as well as Andy Crane for his amazing technical support.

I especially want to thank Dr. Yanting Wang from the Naval Research Laboratory, who is a former student, then a research associate at Colorado State University, for his critical contributions to the early stage of this work and for great discussions with him.

Last but not least, I would like to thank my family members and friends in China for their encouragement, which has helped me get through all the challenges in my life during the past several years.

This research was supported by the National Science Foundation Engineering Research Center Programs.

DEDICATION

To my parents: Yuying Liu and Shuangyue Chen, and my sisters: Dr. Xudong Chen and Xuhong Chen.

TABLE OF CONTENTS

LIST OF TABLES

LIST OF FIGURES

CHAPTER 1

INTRODUCTION

1.1 CASA Background

The United States National Science Foundation Engineering Research Center (NSF-ERC) for Collaborative Adaptive Sensing of the Atmosphere (CASA) is dedicated to revolutionizing our ability to observe, understand, predict, and respond to hazardous weather events using a dense network of small, low-power, and low-cost X-band radars that can collaboratively and adaptively sense the lower atmosphere [1].

Conventional weather radar networks are designed for observing weather events hundreds of kilometers from the radars. A typical example of such a network is the Weather Surveillance Radar-1988 Doppler (WSR-88D or NEXRAD) network jointly owned by the National Weather Service (NWS), Federal Aviation Administration (FAA), and Department of Defense (DoD). The networks use data collected by high-power, long-range radars operating at the S band (about 10 cm wavelength). The NEXRAD network provides radar data with updates every five to six minutes across the United States. However, the networks' spatial resolution and temporal sampling are limited because of earth curvature, ground clutter, and low scan speed, which means that NEXRAD observes the majority of precipitation and wind events only in the middle to the upper troposphere. For example, at the maximum NEXRAD range of about 230 km and assuming a $0°$ elevation angle, the beam is at a height about 3.4 km above ground level (AGL) because of the effect of earth curvature. In addition, current regulations limit the lowest elevation angle used by NEXRAD to $0.5°$. Thus, much of the lower atmosphere (1-3 km AGL) will not be observed by NEXRAD. To overcome the fundamental coverage limitations of today's weather surveillance radars, CASA deploys a series of X-band radars over short ranges to conduct its weather surveillance, monitoring, and prediction. CASA radars are located just few tens of kilometers away from each other and they provide high-resolution dual-polarimetric measurements of the atmosphere close to the ground, with suitable spatial range to facilitate better observation and study of severe weather events. Besides networking small high-frequency radars to overcome the deficiencies of earth curvature and resolution issues, CASA also employs an on-demand adaptive operation architecture to improve its weather sensing and warning systems [1]. To demonstrate its operational methodologies, CASA deployed its first test bed, known as Integrative Project 1 (IP1), in southwestern Oklahoma in fall 2006. Figure 1.1 shows the layout of the CASA IP1 radars. In spring 2012, the CASA IP1 radars were moved to the Dallas-Fort Worth (DFW) metropolitan area to form part of the DFW Urban Demonstration Network. In total, eight dual-polarization X-band radars will be deployed in this urban remote sensing network to demonstrate improved hazardous weather forecasts, warnings, and responses in a densely populated environment. Figure 1.2 is a possible layout of the eight radars. More details about these two testbeds will be presented in Chapter 2.

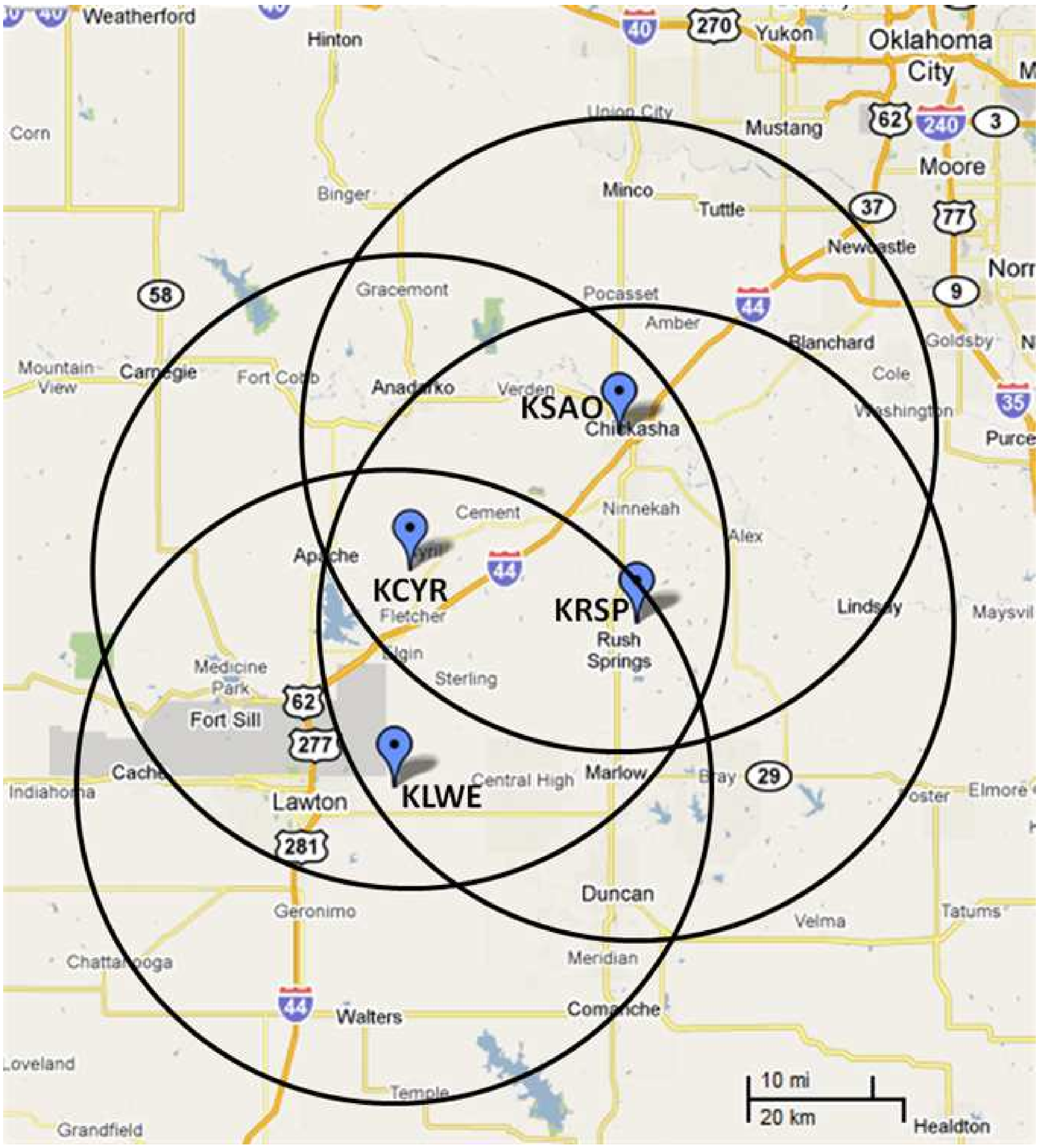

Figure 1.1: CASA IP-1 Radar layout.

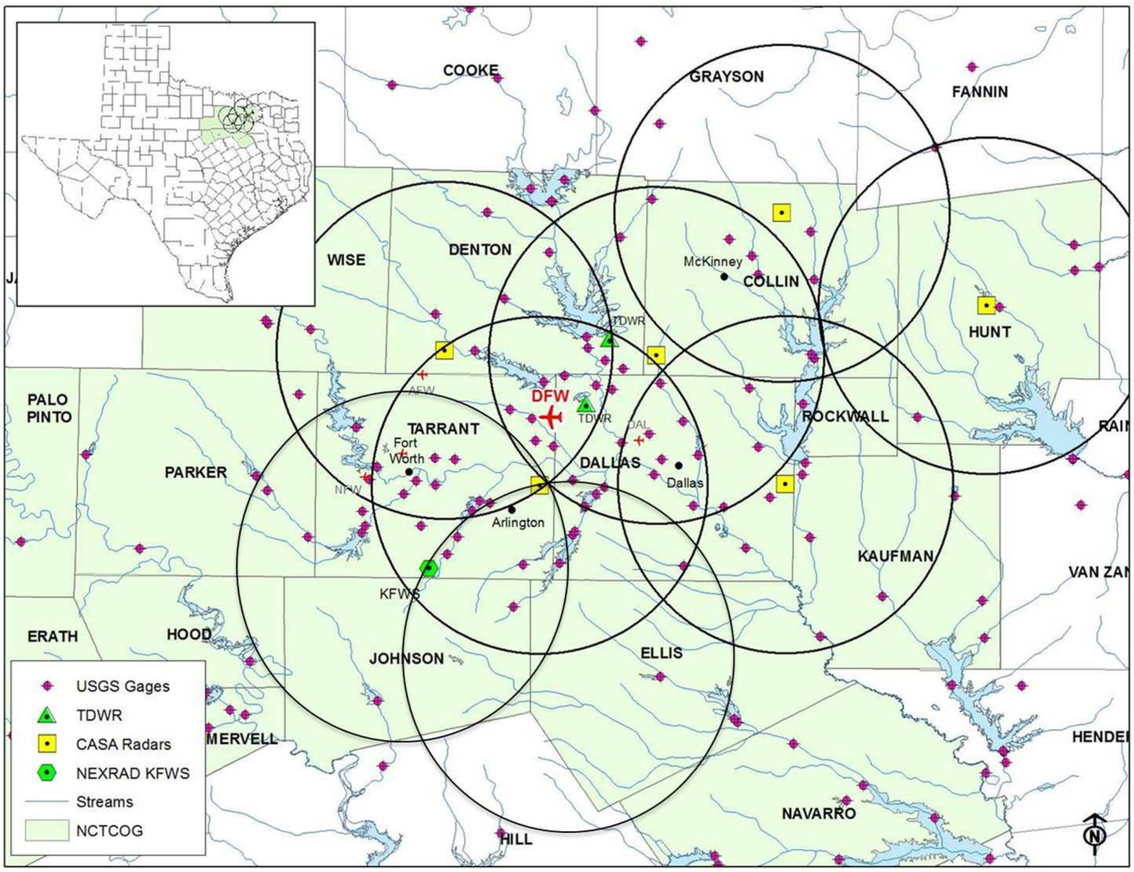

Figure 1.2: DFW urban demonstration network.

CASA is a collaboration among four core academic partners: Colorado State University, the University of Massachusetts (lead institution), the University of Oklahoma, and the University of Puerto Rico at Mayagez. Other collaborating academic institutions include the University of Delaware, the University of Virginia, McGill University, Indiana University of Pennsylvania, and the University of Colorado at Colorado Springs. Some industry and government partners are Vaisala, Raytheon, NOAA, ITT, OneNet, EWR Weather Radar Systems, ParoScientific, Inc., KWTV-NEWS 9 of Oklahoma, and the National Research Institute for Earth Science and Disaster Prevention (NIED) of Japan. For more information one can consult the official CASA Web homepage: $http://www.casa.umass.edu/$.

1.2 Focus of Thesis

The measurement of rainfall rate and amount is critical to a wide range of applications including space and atmospheric sciences, environmental and agricultural research, hydrology, and water resources management. The point observations based on traditional rain gauges have many limitations because of the spatial and temporal variability of precipitation. In the past two decades, the use of radar has greatly changed quantitative rainfall estimation (QPE) by providing spatially continuous estimates of rainfall at small temporal sampling intervals. This now serves as the primary rainfall observing system in many places around the world, with the usage of rainfall gauge measurements for bias corrections, and for merging with the radar estimates. Dual-polarization techniques offer advantages for weather radar applications, including QPE. Dual-polarization radar QPE is one of the most important accomplishments of CASA. This thesis will describe the foundations of radar rainfall estimation, particularly from the perspective of dual-polarimetric techniques. The radar QPE system developed by CASA, including its implementation, ground validation, and performance evaluation, will also be presented in detail.

1.3 Outline of Thesis

This thesis is organized as follows. In Chapter 2, we present the operation methodologies of the CASA X-band radar network, starting with a review of radar basics. Some major accomplishments and breakthroughs of CASA after five years' operation are also described.

In Chapter 3, an overview of existing radar quantitative precipitation estimation algorithms is provided. We then primarily focus on the K_{dp}-based radar QPE system developed by CASA, including various operational considerations of the CASA QPE system, the adaptive estimation of K_{dp}, and ground validation and performance evaluation of the CASA QPE products.

In Chapter 4, we present a five-year validation study of the CASA QPE system. Radar data collected from 40 storm events that happened during years 2007 - 2011 are used for validation and evaluation purposes. Sample real-time products, including high-resolution rainfall maps and point-wise line traces of rainfall estimates, are given. Of course, the performance evaluation results are presented. It is shown that the proposed CASA QPE methodology has greatly improved the accuracy of rainfall estimates compared with current methodologies.

Chapter 5 includes the study's conclusion and comments on future work on the CASA radar quantitation precipitation research. A tentative proposal for how to conduct and extend this research in CASA's urban demonstration network (i.e., the DFW urban remote sensing network) is made.

CHAPTER 2

CASA RADAR NETWORK OPERATION

2.1 Radar Basics

RADAR is a abbreviation of the words **RA**dio **D**etection **A**nd **R**anging. It is an electromagnetic system widely used to sense the position, velocity, and scattering properties of various point or distributed targets. Radar operates by transmitting a particular type of waveform, a pulse-modulated sine wave or square wave, for instance, and detecting the properties of the returned signal [2]. Although radar was first developed as a detection system to warn of approaching hostile aircraft and direct anti-aircraft weapons, today it has become a very common tool in many areas besides defense, such as air traffic control, space science, meteorology, and navigation. One of the two milestones worth mentioning in the history of radar development is that E. V. Appleton and M. A. F. Barnett invented the first device for detecting an object by continuous wave (CW) on December 11, 1924 [3]. The other is that G. Breit and M. A. Tuve successfully detected an object by transmitting a pulse signal in 1925 [4]. A pulse radar system works by transmitting a sequence of short pulses of radio frequency (RF) energy and then listening for its echo off distant objects. Pulse radar needs more complex technologies than continuous wave radar, but it is more efficient and powerful.

A basic capability of almost all radars is estimating the radial distance between a monostatic radar and a target. The total distance from radar transmitter to the target and back to the radar receiver is equal to the product of the speed of light, c, and the round trip time, t, because the electromagnetic energy propagates at the speed of light (3×10^8 m/s). Theoretically, the radar-target radial range R should be

$$R = \frac{ct}{2} \tag{2.1}$$

However, meteorological targets such as fog, clouds, rainfall, and snowfall are generally composed of a large number of hydrometeors moving with different velocities and extending over a large range with widely different scattering amplitudes. The pulse radar system senses them as distributed targets within a sample volume, which is defined by the radar's vertical beamwidth, θ, and horizontal beamwidth, ϕ, extending a sample range, $\triangle r$ (see Figure 2.1). The horizontal/vertical beamwidths are parameters based on the physical properties of the radar antenna. The sample range dimension, $\triangle r$, is dependent on the pulse width, T_0, by the relationship as

$$\triangle r = \frac{cT_0}{2} \tag{2.2}$$

The pulse width, T_0, is also often called pulse duration.

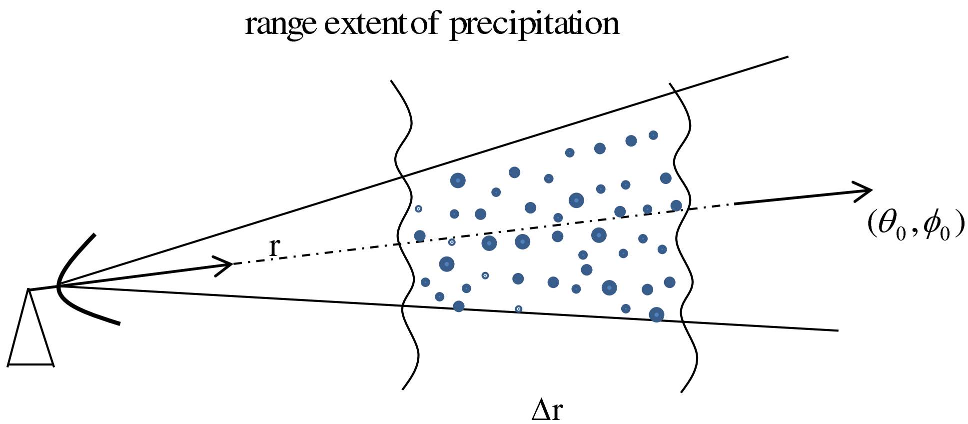

Figure 2.1: Distributed targets in a sample volume.

The above relationship can be explained by the properties of a finite-duration pulse in the range-time domain, as shown in Figure 2.2. The leading and trailing edges of a transmitted radar signal can be characterized as two lines defined by $r = ct$ and $r = c(t - T_0)$, respectively [5]. The returned signal/power at the radar receiver at time $t^{'}$ consists of contributions from all the particles in the range between r_1 and r_2, which are located along the characteristic line whose slope equals $-c$. Obviously, the sample range $\triangle r = r_2 - r_1$. The $\triangle r$ is often referred to as the finest theoretical range resolution cell of a radar system. A well-designed radar should be able to distinguish targets separated by $T_0/2$, which indicates that the pulse width is the dominant factor of the radar range resolution. The time period between each transmitted pulse T_s in Figure 2.2 is known as the pulse repetition time, or PRT. The reciprocal of pulse repetition time is called the pulse repetition frequency, or PRF.

Another important characteristic of a pulse radar is its maximum unambiguous range, r_{max}, which is also illustrated in Figure 2.2. r_{max} essentially represents the maximum range a radar pulse can travel and return before the next pulse is sent out. It is defined as

$$r_{max} = \frac{cT_s}{2} \tag{2.3}$$

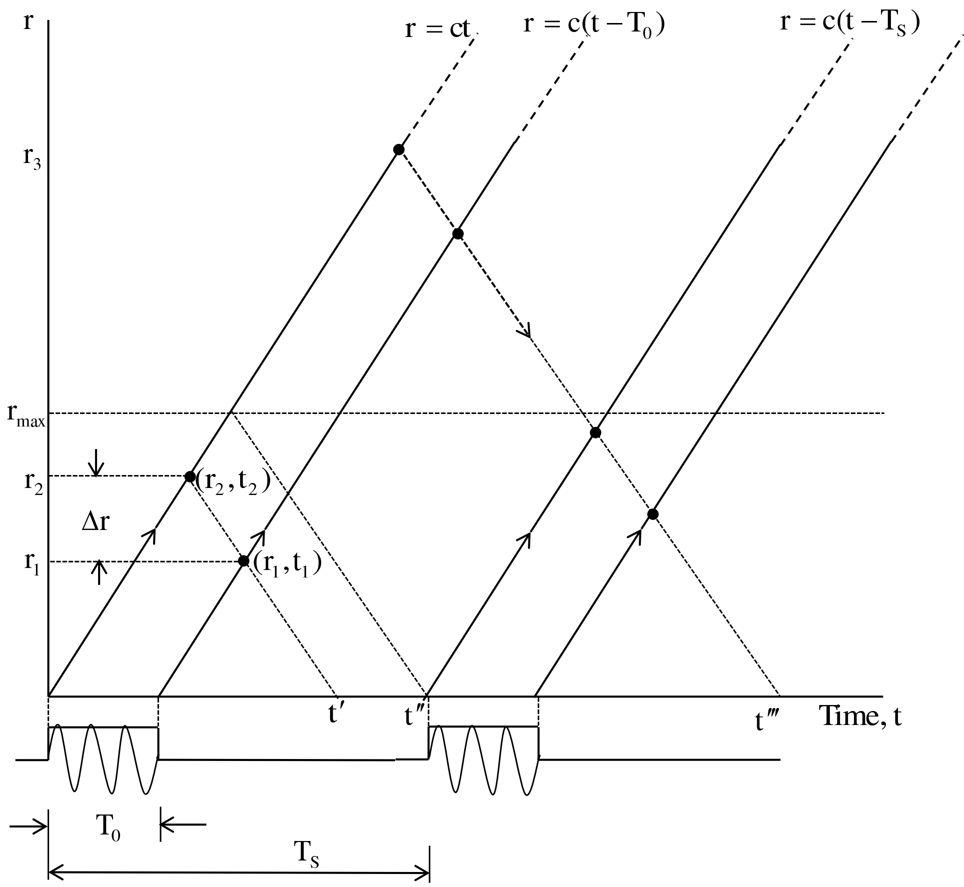

Figure 2.2: Range-time characteristics of a pulse radar system.

Of course, the radar can detect targets beyond r_{max}, but in this case the reflected signal would be aliased with echoes from the next pulse and even more following pulses, making its range ambiguous. For example, at time $t^{'''}$ in Figure 2.2, the returned power contains reflected signals from the given two pulses. This phenomenon is known as range folding or the second-trip echo. An obvious method to resolve this issue is to increase r_{max} by increasing the pulse repetition time, but this will conflict with the availability of maximum unambiguous velocity V_{max}, which the radar can determine for a volume of targets. Based on the effect of Doppler shift, the mathematical relationship between unambiguous velocity and the pulse repetition frequency can be expressed as

$$V_{max} = \frac{\lambda * PRF}{4} \tag{2.4}$$

where λ is the radar wavelength.

Recalling equation 2.3, we can see that both r_{max} and V_{max} have a direct relation with the PRF. That is, r_{max} has an inverse dependence on the PRF, whereas V_{max} has a direct dependence. An increase in the PRF will result in an increase in V_{max} , but a decrease in r_{max}. On the other hand, a decrease in the PRF will result in a decrease in the V_{max} but an increase in the r_{max}. Although a high V_{max} is preferable for obtaining high-quality Doppler velocity information, this will come at the expense of using a high PRF, resulting in a shorter unambiguous range, which may increase the chance of multiple trip echoes. This contradiction is often called the *Doppler Dilemma*.

Pulse-Doppler radars essentially sample the atmospheric information with its PRF as the sampling frequency. Usually, the pulse rate is many orders of magnitude faster than the mechanical scanning motion even for the cases when the radars are scanning quickly across a wide arc [8]. This will lead to a truth that each sample volume is actually time-sampled hundreds of times. In this discrete time-sample mechanism, each sample is an observation of the underlying random process taking place at the corresponding volume. Numerous time-samples of the volume will form the fundamental unit of radar observation, known as a range gate or range bin. A beam/ray can be generated from many range bins of a particular radar azimuth; a sweep will be formed from the many rays of different azimuths; and multiple sweeps across different elevations and/or azimuths will form a volume. This strategy is often called a radar volume scan.

For most meteorological radars, the received signal is output as in-phase and quadrature components, which are also called I and Q components, or time series data. The time series (I and Q) values can be used to calculate the moment data such as radar reflectivity, mean Doppler velocity, spectrum width, and dual-polarization parameters like differential reflectivity (Z_{dr}) and differential propagation phase (ϕ_{dp}). The moment data are critical for further applications, including rainfall estimation and vector wind retrieval. From Bringi and Chandrasekar (2001) [5], the I and Q components for a pulse Doppler radar can be expressed as,

$$I(t) = A\cos(2\pi f_0 \tau)U_{tr}(t-\tau) \tag{2.5}$$

$$Q(t) = -A\sin(2\pi f_0 \tau)U_{tr}(t-\tau) \tag{2.6}$$

where U_{tr} is the transmitting waveform.

The details of weather radar system design and signal processing are beyond the scope of this thesis. However, one can refer to an excellent book on the principles and applications of polarimetric Doppler meteorological radar ([5]: chapter 5).

2.2 CASA DCAS Observation Methodology

CASA has proposed a new atmospheric sensing paradigm called DCAS, distributed collaborative adaptive sensing, to adaptively and collaboratively operate the radar network according to real-time changing atmospheric conditions, prevailing weather information, and the needs of various end users [6]. Specifically, "distributed" refers to the use of a large number of small X-band dual-polarization radars to overcome the earth-curvature blockage and make up the resolution degradation caused by spreading of radar beams at long ranges and large temporal sampling intervals of the current operational S-band radar network, i.e., the WSR-88D Next Generation Doppler Radar (NEXRAD). These smaller and less-expensive radars have a circular shape coverage area with a radius of about 40 km and they are deployed about 30 km away from each other, which is much closer than in the NEXRAD network. And they operate "collaboratively" through the proposed detecting, tracking, and predicting schemes. "Adaptive" refers to the dynamic interactions among the radars, changing atmospheric conditions, prevailing weather information, the associated computing and communications infrastructures, and the needs of various end users. Overall, a DCAS system should include remote sensors, algorithms that detect and predict hydrometeorological hazards such as tornadoes and heavy storms, an underlying substrate of distributed computation that dynamically processes the collected data and manages system resources, and interfaces that enable end-users to access and interact with the system. The main goal of such a DCAS system is to save lives and reduce property loss through improving precipitation estimates for flood prediction as well as reducing the tornado false alarm rate. For instance, while providing quantitative precipitation estimation (QPE) information, the DCAS system is able to track tornadoes for public warning and emergency management (EM). Figure 2.3 is a flow chat showing the DCAS methodology from a systematic perspective.

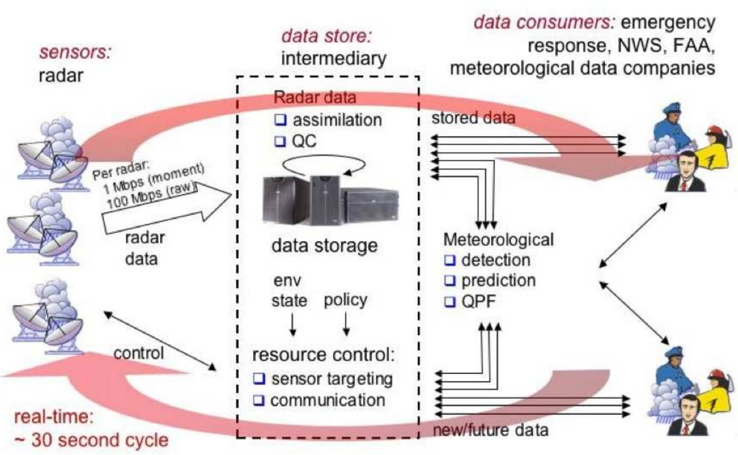

Figure 2.3: Distributed collaborative adaptive sensing (DCAS) system driven by end-user data need.

2.3 CASA IP1 Test-bed Overview

The Integrated Project 1 (IP1) is the first test bed developed by CASA. It served as a prototype for a DCAS system to achieve high temporal and spatial resolution sensing of winds in the lower atmosphere and the detection, tracking, and anticipation of severe storms, especially fast-formed tornadoes. The location of the test bed was chosen for its climatological and meteorological properties. The IP1 test bed was located approximately 30 miles southwest of Oklahoma City, covering a 7,000 km^2 region that receives an average of four tornado warnings and 53 thunderstorm warnings per year. Being in Tornado Alley, the test bed has about a 77% chance of experiencing at least one tornado in each year, and severe storms are almost 100% guaranteed every year. The test bed is a network consisting of four mechanically scanning, automated, short-range X-band, magnetron radars with overlapping coverage domains in southwestern Oklahoma. As shown in Figure 1.1, these radars, namely, KCYR, KLWE, KRSP, and KSAO, were located near the towns of Cyril, Lawton, Rush Springs, and Chickasha, respectively. Table 2.1 lists the specifications of the CASA IP1 radars. The IP1 radars are also under the NEXRAD coverage of the KFDR and KTLX radars, as shown in Figure 2.4.

Table 2.1: Specifications of CASA radar.

Transmitter	
Type	Magnetron
Center Frequency	9410± 30 MHz
Peak Power Output	8.0 kW (per channel)
Average Power Output	12 W (per channel)
Pulse Width	660-1000ns
Polarization	Dual Linear (Horizontal and Vertical)
Max Duty Cycle	0.16%
Receiver	
Type	Dual-channel linear output I/Q
Dynamic Range (BW=1.5MHz)	103 dB
Noise Figure	5.5 dB
Antenna and Pedestal	
Diameter	1.2 m (Dual-polarized parabolic reflector)
3-dB Beamwidth	1.8°
Azimuth Scan Rate	up to 240°/s
Elevation Scan Rate	up to 30°/s
Acceleration	up to $120°/s^2$
Data Acquisition System	
Sampling Rate	100 MSps
Dynamic Range (bandwidth = 1.5 MHz)	108 dB
Data Transfer Rate	88.3 Mbps
Decimation Factor	Adjustable
Video Bandwidth	Adjustable

The four IP1 radars were scanning collaboratively and adaptively under the direction of the Meteorological Command and Control (MC&C) system that performs the system's main control loop, including ingesting data from the remote radars, identifying meteorological features from the ingested data, reporting features to end-users, and determining each radar's future scan strategy based on detected features and

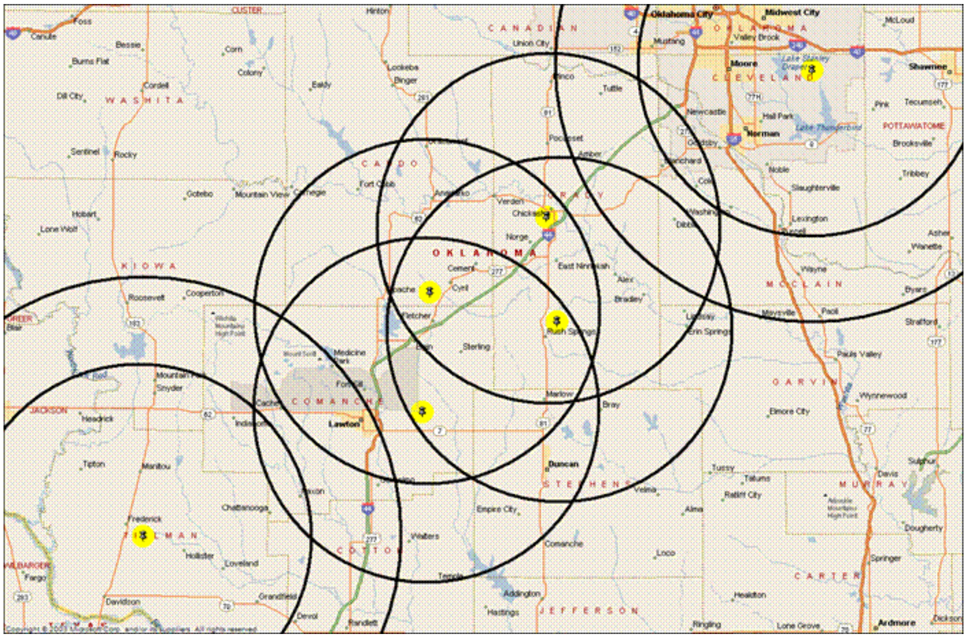

Figure 2.4: The layout and location of the IP1 weather radar network. The coverage circles of the IP1 radars are in a radius of 40 km. KTLX is to the northeast of the test bed and KFDR is to the southwest of the test bed, both shown with 40 km and 60 km ranges, as indicated.

end-user requirements. The MC&C is executed at a central control site known as the System Operation and Command Center (SOCC) in the University of Oklahoma. IP1 can be regarded as a closed loop from the sensing radars through the computing and communication infrastructure and algorithms because the sensing resources dynamically adapt to end-user needs and preferences.

2.4 Dallas-Fort Worth Test-bed Overview

From spring 2012, CASA, in collaboration with the North Central Texas Council of Governments (NCTCOG), the National Weather Service (NWS), and some other stakeholders, has embarked on a project to create the DFW Urban Demonstration Network to demonstrate improved forecasts, warnings, and responses in a densely populated urban environment. Centered in the demonstration test bed will be a network of eight boundary-layer observing, dual-pol, X-band radars. The systems to be implemented in this urban test bed are based on the new technologies and end user research developed by the CASA project. The DFW remote sensing network is regarded as the first urban weather demonstration network in the United States.

The issues to be addressed include (1) a development of high-resolution, two- and three-dimensional mapping of current atmospheric conditions focusing on the boundary layer to sense, detect, and forecast low-level wind, tornado, hail, ice, and urban flooding hazards; (2) creation of impacts-based, neighborhood-scale warnings and forecasts for a range of public and private decision-makers that result in measurable benefits for public safety and the economy; (3) demonstration of the value of collaborative, adaptive X-band radar networks to existing and future sensors, products, performance metrics, and decision-making; and assessment of optimal combinations of observing systems; (4) development of models for federal/municipal/private partnerships to introduce new observation technologies for ongoing operational and interdisciplinary weather system research. Data products will include single and multi-radar data, vector wind products, model- based assimilated data, QPE, nowcasts, numerical weather prediction products, and so forth.

This urban demonstration network is supposed to cover 12 out of the 16 counties in the DFW area, providing coverage to most of the 6.5 million people in this region. In addition, the existing in situ and remote sensors, such as WSR-88D, TDWR, and rain gages will be used for creating new products and for validation purposes. This partnership and test bed are expected to be a prototype of a national-scale "network-of-networks" in which different users and data providers can exchange observational data across a common infrastructure. The initial four radars, which are also the CASA IP1 radars moved from Oklahoma to Texas, have been refurbished and installed in the metroplex. Figure 2.5 shows the layout of the initial 4 radars.

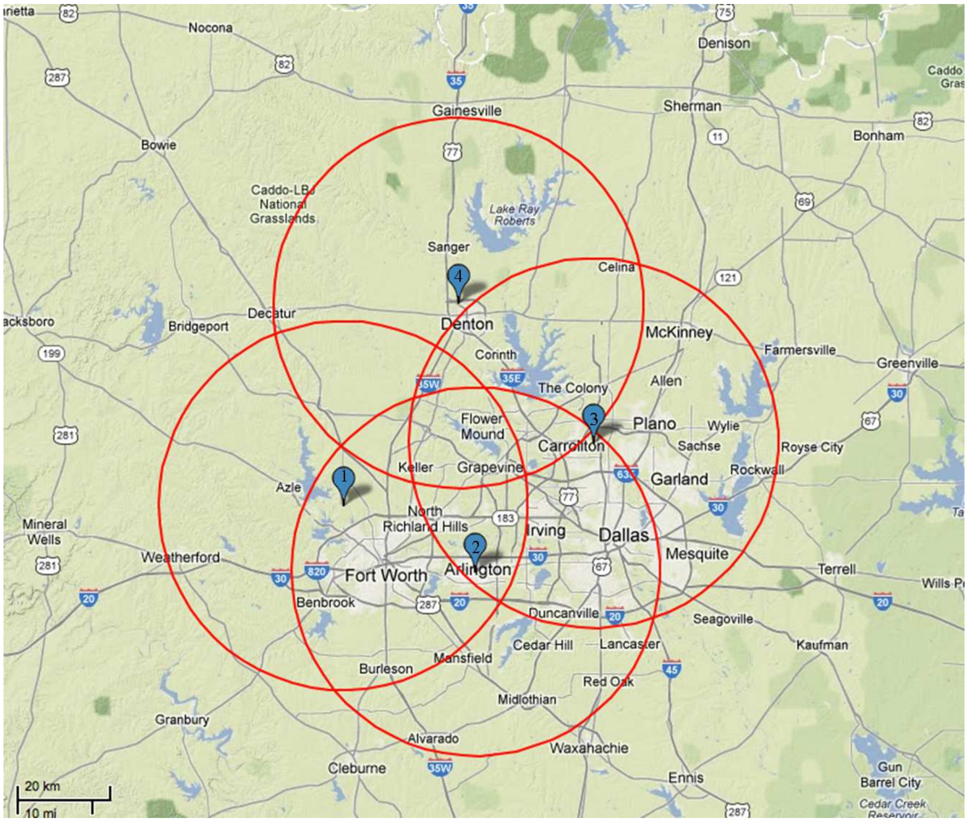

Figure 2.5: Layout of the initial 4 radars in the DFW test bed.

The locations of the four radars in lat/lon are: radar 1 (Lat: 33.2536, Lon: -97.152), radar 2 (Lat: 32.9814, Lon: -96.8391), radar 3 (Lat: 32.7306, Lon: -97.1125), and radar 4 (Lat: 32.8368, Lon: -97.4257).

2.5 CASA Accomplishments and Breakthroughs

From 2007 to 2011, a series of spring experiments were conducted in CASA's IP1 test-bed. The 5-year operation demonstrated the key features of the CASA DCAS concept, including that (1) a short-range X-band radar network can be configured as an adaptive system to provide high-quality severe weather observations; (2) such a network can provide higher-resolution views of the lower atmosphere than large S-, or C-band radars; (3) a shared radar operation system can satisfy the multiple data usages for different uses. The first two years' field experiments were mainly focused on the validation of the test-bed itself, whereas in the storm season of 2009, 2010, and 2011, different precipitation types and tornadoes that occurred in the IP1 test bed were successfully detected and tracked with excellent spatiotemporal resolutions by the CASA DCAS system. In this section, the major accomplishments and breakthroughs during the five-year' deployment will be summarized. Some related topics and results can be found in various CASA publications.

2.5.1 Networked Reflectivity Acquisition

Traditionally, data processing is done at each single radar node using the radar-centered coordinate system, where multiple views of a common radar volume are merged as a "mosaic". In CASA the DCAS system, a new reflectivity and attenuation retrieval method, was invented to take advantage of the observation diversities within the radar network. Combining the forward scatter and back scatter equations of the precipitation medium with total path attenuation constraints, the reflectivity field and specific attenuation along each beam can be accurately estimated. In addition, the attenuated observations through multiple paths are used simultaneously to retrieve the intrinsic reflectivity [7]. The biases evaluation results for both simulations and real data tests done by CASA have demonstrated good accuracy of the retrieval method [7]. Also, the algorithm was successfully tested for real-time implementation.

2.5.2 Multi-Doppler Vector Wind Retrieval and Tornado Tracking

Doppler weather radars are often the preferred tools for air motion retrieval because of their capability of 3D coverage. However, multiple Doppler radar products are not very feasible since most of the current operational WSR-88D systems do not have significant overlap. CASA has developed a real-time multi-Doppler retrieval system that was implemented in the DCAS network. This multi-Doppler system can produce precise vector wind observations and has a strong ability to detect convective cells and tornadoes. The 3D wind vector products are generated in accordance with the networked sensing modes to take advantage of the overlapping coverage for multiple-Doppler synthesis, while still maintaining a high enough resolution to capture the detailed synoptic features. Figure 2.6 shows the retrieved wind vectors along with the reflectivity profiles at two sample time frames for a strong tornado that happened on May 24, 2011.

There are two main components in the real-time multi-Doppler system: data interpolation and Doppler synthesis module. Both of them are composed of new and legacy software controlled by the Perl meta-script. These modules were implemented based on the retrospective programs known as REORDER and CEDRIC, which were developed by the National Center for Atmospheric Research (NCAR) for the specific purpose of gridding radial data onto a common Cartesian space and performing multi-Doppler synthesis.

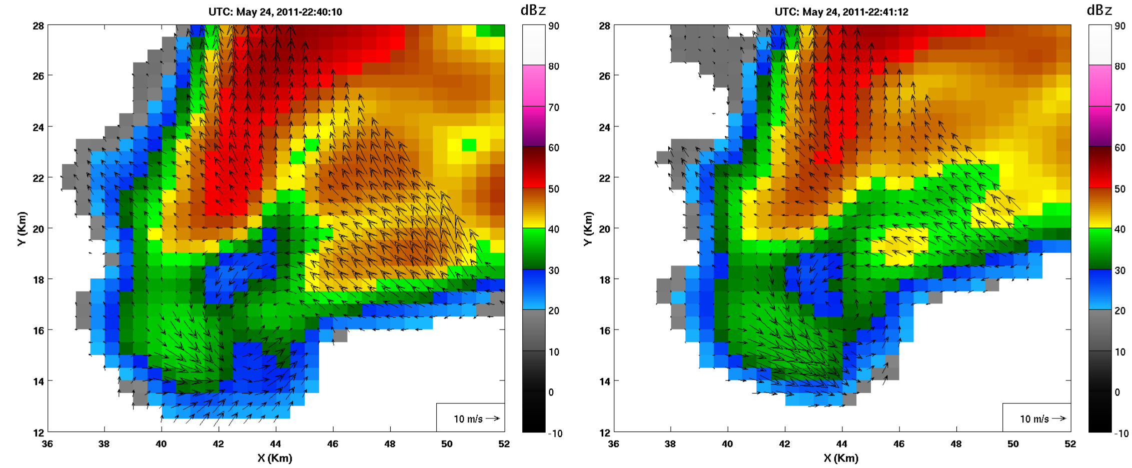

(a) UTC: 22:40:10 (b) UTC: 22:41:12

Figure 2.6: EF-4 Tornado touchdown on May 24, 2011 (the lat/lon information of origin (0 km, 0 km) is (34.8276°, -98.1007°))

.

The first subsystem of the multi-Doppler system is a nc2uf format conversion program that converts the archived CASA NetCDF format data to Universal Format (UF) which can be ingested by the software REORDER [8]. Then, the REORDER subprogram will grid and interpolate the UF volumes from their radial dimensions to Cartesian coordinates through range-weighted averaging of range gates to single grid points. Subsequently, the subroutine CEDRIC will synthesize the gridded volumes from each radar into a single composite grid with resolved u, v, and w fields. The CASA multi-Doppler system has been tested and validated in the IP1 test bed, and the data collected for 2009 and 2010 weather events were also used for post-processing. For a detailed description of the real-time retrieval system and its implementation procedure, including the establishments of the two main components, one can refer to Sean Zhang's work [8].

Using the high-resolution vector wind products observed close to the ground, the CASA DCAS paradigm can also detect and track tornadoes. This capability was clearly demonstrated during a group of violent EF-4 tornadoes led by strong upper-level dynamics and a warm, moist surface layer within the IP1 network on May 24, 2011. The storms entered the network from the southwest and later spawned several tornadoes that affected several towns like Chickasha and Lookeba, Oklahoma. The hook echoes and wind rotations were clearly seen from the CASA real-time display, which helped the weather service and emergency management issue a tornado warning and confirm the tornado touchdown. The vorticity was calculated from the horizontal wind fields and its peaks were used to locate the damage path. Figure 2.7 illustrates the path of two tornadoes that occurred on that day. This demonstrated the capability of DCAS observations for tracking tornadoes down to the street, with higher resolution and lower level coverage, and the potential to improve tornado warnings.

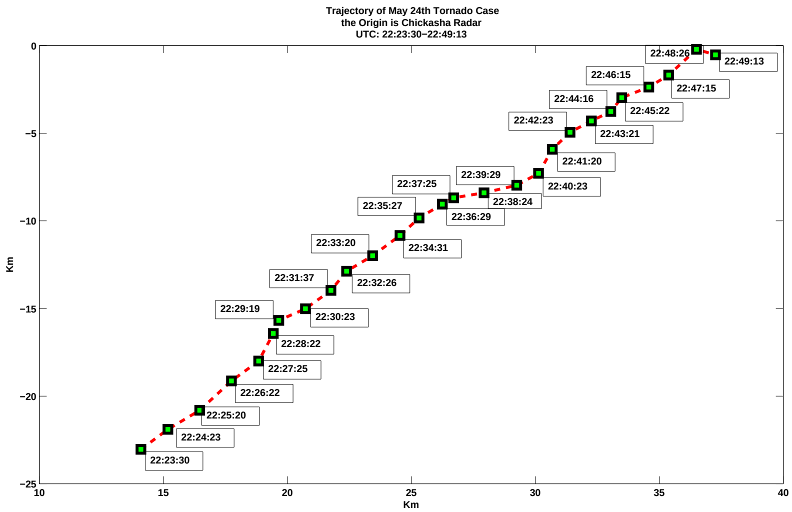

(a) Hook 1

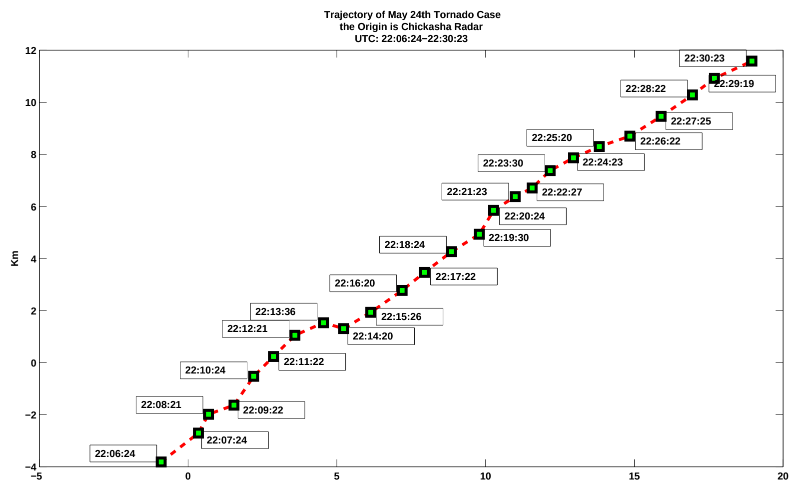

(b) Hook 2

Figure 2.7: Paths of the EF-4 tornadoes that occurred on May 24, 2011

.

2.5.3 Nowcasting System

To provide short-term forecasting, also known as nowcasting, of severe weather events, especially tornadoes and flash floods, a nowcasting method consisting of a Fourier-based dynamic adaptive radar tracking of storms (DARTS) algorithm for motion estimation has been developed over an innovative space-time model and spectral domain solver. The DARTS system can predict weather phenomena up to a 20-minute lead time, and it was further enhanced by adapting the current state-of-the-art scale filtering techniques. In addition, the implementation of the DARTS nowcasting system into the closed loop can predict the reflectivity fields during fast-moving weather events, which will give a better estimation of storm locations for scan optimization. In this way, the DCAS scans are able to capture the leading edge of moving rainfall storms. Details about the CASA nowcasting system can be found in the work done by Ruzanski et al. [9].

2.5.4 Users' Evaluation and Decision-Making

The archived dual-polarization CASA X-band radar data was used by the National Weather Service (NWS) forecasters to measure the impacts of CASA's high-resolution, lower troposphere data on their weather forecasting models and wind predictions. For example, a severe thunderstorm warning will be issued when NWS forecasters expect a wind speed over 58 mph. It was found that the usage of CASA together with NEXRAD data could made wind assessments about 30% more accurately in terms of mean absolute error than assessments made by the NEXRAD data only [10]. A good example that shows the advantage of using CASA data is the observation of a tornado that touched down near Chickasha, Oklahoma, on May 24, 2011. Both CASA and NEXRAD radar systems were used to monitor the storm formation. The National Weather Service radar showed the tornado would cross the southern part of Newcastle about 25 miles up Interstate 44, and officials sent emergency crews to that part of the city. However, as the tornado approached Newcastle, the emergency manager, based on the frequently updated CASA data, found that the tornado was actually making a turn to the north. With that information, forecasters could issue warnings more often and make correct decisions.

2.5.5 Quantitative Precipitation Estimation and Forecasting

Quantitative precipitation estimation (QPE) is an important application of weather radar engineering and a powerful tool for forecasting flooding risk. QPE and QPF are also critical components of the CASA DCAS architecture. A high spatial and temporal resolution rainfall estimation methodology has been developed during observations made over the past several years. The radar polarimetric data-based algorithms were implemented at the central node in CASA's IP1 test bed. Once storm cells are detected, the QPE module will be activated to produce a rainfall map in real time based on the fast scan strategies.

In addition, the excellent performance of the DARTS nowcasting model in processing the high-resolution CASA radar reflectivity data encourages the usage of specific differential phase data retrieved from CASA X-band dual-polarization radars for rainfall field nowcasting [12]. The CASA QPE and/or short QPF products will drive the high-resolution hydrologic integration into the DCAS network to predict runoff response, especially at the urban drainage networks of particular interest, to significantly improve the applications for flood warning, mitigation, and advisories, especially for fast-developing urban flash floods. In general, being an end-to-end system, DCAS will combine several functions into an integrated program, including data fusion, rainfall estimation, short-term precipitation forecast, and user impacts, as well as people's responses. Details about the CASA QPE system will be given in the following chapters. One can refer to Ruzanski and Chandrasekar's work [12] for more information about rainfall field nowcasting.

2.6 Summary

A brief review of radar basics was presented in this chapter. The CASA DCAS scanning methodology was then extensively described, including the description of CASA's two test beds. The chapter ended with highlights of CASA research topics.

CHAPTER 3

RADAR QPE ALGORITHM DESCRIPTION

3.1 Overview of Current QPE Algorithms

Estimation of rainfall rate and amount has been important since the beginning of civilization. Radar is a powerful tool for measuring rainfall because it can observe precipitation over a wide area in a relatively short period of time and it can provide advanced warning of precipitation systems that will impact a region. Radars have been used for detecting precipitation echoes since the beginning of World War II. And radar QPE can be traced back to the work done by Wexler [13] and Marshall et al. [14]. Cifelli and Chandrasekar classified the factors influencing radar QPE into two broad categories, basic science aspect and applied engineering aspect [15]. Both the basic science and engineering issues should be addressed in order to accurately estimate rainfall. A detailed accounting of the various factors classified as basic and physical science issues affecting radar quantitative precipitation estimation was presented in [15]. This section will provide an overview of current radar QPE algorithms, including description of different raindrop size distribution (DSD) models and different parameter-based rainfall algorithms.

3.1.1 Raindrop Size Distribution (DSD)

Raindrop size distribution describes the probability density distribution function of raindrop sizes, which forms the building blocks for deriving physically based rainfall algorithms. Understanding the properties of DSD variability, and determining whether they are random or associated with specific physical processes, can lead to a better perception of microphysical and dynamic cloud processes involved in the generation of precipitation particles. A good knowledge of the DSD in the precipitating system is critical for radar QPE and QPF. Different rainfall algorithms can be developed based on different DSD models, using radar observations such as reflectivity, differential reflectivity, and/or specific propagation phase. DSD information is also critical for rainfall field simulation research.

Since the early work of Marshall and Palmer [16], various DSD models (e.g., [17] [18] [19]) have been proposed. Following are some commonly used DSD models in real applications.

3.1.1.1 Gamma Distribution

The gamma raindrop size distribution can be expressed as [5],

$$N(D) = n_c f_D(D) \tag{3.1}$$

where D is the raindrop diameter in mm, $N(D)$ is the number of raindrops per unit volume per unit size interval (D to $D + \triangle D$) with a unit of $\mathrm{m}^{-3}\mathrm{mm}^{-1}$, n_c is the concentration, and $f_D(D)$ is the probability density function (PDF) given by [20],

$$f_D(D) = \frac{\Lambda^{\mu+1}}{\Gamma(\mu+1)} \exp^{-\Lambda D} D^{\mu} \tag{3.2}$$

where Λ and μ ($\mu > -1$) are parameters of the gamma PDF.

Other gamma distribution models can be derived from the above description of drop size distribution. One model worth mentioning was proposed by Ulbrich [18], where DSD was expressed as a modified gamma function of the form

$$N(D) = N_0 D^{\mu} \exp(-\Lambda D) = N_0 D^{\mu} \exp(-(4+\mu)\frac{D}{D_m}) \tag{3.3}$$

Again, D is the diameter, μ denotes the shape parameter, N_0 is the scaling parameter, whereas D_m is the mass-weighted mean diameter defined as

$$D_m = \frac{\int D^4 N(D) dD}{\int D^3 N(D) dD} \tag{3.4}$$

and Λ is the slope parameter related to D_m by $\Lambda = (4+\mu)/D_m$.

If μ is a positive value, $N(D)$ will decreases as the diameter decreases, causing a downward curvature of the number concentration ($N(D)$) at small raindrop sizes, whereas the number concentration will increase as the diameter decreases if μ has negative values [21]. Theoretically, the number of concentrations has a mathematical infinite value with zero diameter. Illingworth and Blackman concluded that radars that observe the raindrops within the Rayleigh scattering region cannot resolve the small raindrops, and a fixed value of the shape parameter is appropriate for describing the DSD when using meteorological radars [22]. For instance, μ can be set to a constant value such as 2.5 or 5 in the gamma distribution (equation 3.3) [22]. In contrast, Brandes et al. [23] and Zhang et al. [24] suggest that the following mathematical relationships can be applied between μ and Λ in the gamma DSD model,

$$\Lambda = 0.0365\mu^2 + 0.735\mu + 1.935 \tag{3.5}$$

Based on the relation $\Lambda = (4+\mu)/D_m$, the above $\mu - \Lambda$ relation can be converted into a $\mu - D_m$ connection, as

$$D_m = \frac{4+\mu}{0.0365\mu^2 + 0.735\mu + 1.935} \tag{3.6}$$

However, the particular $\mu - \Lambda$ relationship could be precipitation type and/or region dependent. More work is needed to validate these relations.

3.1.1.2 Exponential Distribution

The exponential distribution was first proposed by Marshall and Palmer [16], and was used in many studies before Ulbrich [18] introduced the Gamma distribution model. The DSD was then described as a function in the following form:

$$N(D) = N_0 \exp(-\Lambda D) \tag{3.7}$$

Again, D is the diameter, $N(D)$ represents the number of drops per millimetre diameter interval per cubic meter of air, N is a constant of about 8000 m^{-3}mm^{-1}, and Λ is a parameter that depends on the rainfall rate, as

$$\Lambda = 4.1R^{-0.21} \tag{3.8}$$

where R is the rain rate in mm hr^{-1}.

From equations 3.3 and 3.7, it is easy to see that the exponential DSD is actually a special case of the Gamma distribution model when $\mu = 0$, and it can be expressed as

$$N(D) = N_0 \exp(-\Lambda D) = N_0 \exp(-4\frac{D}{D_m}) \tag{3.9}$$

3.1.1.3 Log-normal Distribution

The raindrop size distribution can also be described by a log-normal distribution, as in the research done by Feingold and Levin [25],

$$N(D) = N_t \exp[-ln^2(\frac{D}{D_m})(2ln^2\sigma)] \tag{3.10}$$

where N_t is the total number of drops per unit volume and σ is the width of the distribution. An interesting property of this log-normal distribution is that $N(D)$ will approach zero as the raindrop diameter approaches zero.

3.1.2 Different Rainfall Algorithms

3.1.2.1 Traditional $Z - R$ Algorithm

Traditional rainfall measurements from radars, especially single-polarization radars, often start with this reflectivity-rainfall relation, commonly referred as the $Z - R$ relation. If we let $N(D)$ denote the DSD, where D is the equivalent drop size in diameter, the reflectivity factor Z can be defined as [5]

$$Z = \int_D D^6 N(D) dD \tag{3.11}$$

It is commonly expressed in the units of mm^6m^{-3}. However, the logarithmic transformation $10\log_{10}(Z)$ is often used since the precipitation particles can vary in diameter over many orders of magnitude, and its units are in decibels of Z relative to 1 mm^6m^{-3} (which is 0 dBZ).

The still-air rainfall rate (in mm hr^{-1}) can be written as a relationship [5] with the DSD as,

$$R = 0.6\pi \times 10^{-3} \int v(D) D^3 N(D) dD \tag{3.12}$$

Again, D is diameter in mm, $N(D)dD$ is the number of drops m^{-3} in the interval from D to $D + dD$, and $v(D)$ is the drop terminal velocity (in m/s) at sea level, which depends on parameters such as air density, size and shape of raindrops, etc. The terminal velocity of raindrops can be expressed as a form given by Atlas et. al [26],

$$v(D) = 9.65 - 10.3 \exp(-0.6D) \tag{3.13}$$

or a power law form as

$$v(D) = \alpha D^{\beta} \tag{3.14}$$

where the coefficient α varies from 3.6 and 4.2, and β from 0.6 to 0.67 for precipitation events. For rainfall rate estimations, the most commonly used sea-level values for α and β are 3.78 and 0.67, respectively [27]. Based on this model, radar-based rainfall algorithms can be developed. All the rainfall algorithms described in this chapter are assumed to apply at sea level.

From equations 3.11 and 3.12, it can be seen that both Z and R can be approximated as moments of the DSD. Subsequently, the $R(Z)$ relation can be expressed in a parametric form as

$$Z = AR^b \tag{3.15}$$

where A and b are empirically derived constants. Battan suggested some typical relations as: for thunderstorm rain, $Z = 486R^{1.37}$; for orographic rain, $Z = 31R^{1.71}$; for stratiform rain, $Z = 200R^{1.6}$, [28]. A list of coefficients recommended by the National Weather Service Radar Operations Center (NWS-ROC) for use in the U.S. can be found in Table 3.1.

Table 3.1: Coefficients for usage of $Z - R$ relations.

Usage	**A**	**b**	**Optimum for:**	**Also Recommended for:**
Marshall-Palmer	200	1.6	General stratiform rainfall	-
East-Cool Stratiform	130	2.0	Winter stratiform precipitation (east of continental divide)	Orographic Rain -East
West-Cool Stratiform	75	2.0	Winter stratiform precipitation (west of continental divide)	Orographic Rain -West
WSR-88D Convective	300	1.4	Summer deep convection	Other non-tropical convection
Rosenfeld Tropical	250	1.2	Tropical convective systems	-

Source: $http://www.roc.noaa.gov/ops/z2r\_osf5.asp$

3.1.2.2 R-K_{DP} Approach

With the development of dual-polarization techniques (for instance, the NWS WSR-88D has been upgraded to dual-pol capabilities), we are able to better determine the type and intensity of rainfall. Although fundamental challenges in radar rainfall estimation remain, dual polarization observations offer a number of advantages over single polarization radar rainfall estimation because more information about the drop size distribution (DSD) can be gleaned. In addition, dual-polarimetric estimators can better account for the existence of ice. Furthermore, the radar dual-polarimetric observations also help significantly in discriminating smoke from fires, birds, bats, and bugs. In this section, the K_{dp} based rainfall algorithm will be briefly presented. More information about the CASA QPE methodologies can be found in follow-on sections and/or chapters.

It was shown in [5] that the specific differential propagation phase K_{dp} (in degree km^{-1}) is proportional to the product of rainwater content and the mass-weighted mean diameter of raindrops,

$$K_{dp} \approx (\frac{180}{\lambda})10^{-3}CW(0.062D_m) \tag{3.16}$$

Again, D_m is the mass-weighted mean diameter defined in equation 3.4, whereas W is the rainwater content in units of g/m^3, and λ is radar wavelength in m.

Reusing the relationship between rainfall rate and DSD (equation 3.12), a general $R(K_{dp})$ estimator can be derived in the following form,

$$R(K_{dp}) = aK_{dp}^{b} \tag{3.17}$$

where the constants a and b are dependent on different climatic and synoptic properties.

From equation 3.16, we can see that K_{dp} is inversely proportional to wavelength in the Rayleigh limit for fixed water content and mass-weighted mean diameter. Thus, the K_{dp}-based rain rate estimate can be written as a frequency-scaling form [5],

$$R(K_{dp}) = 129(\frac{K_{dp}}{f})^{c} \tag{3.18}$$

The frequency-scaling argument is generally valid up to 13 GHz [5].

Obviously, the estimation of K_{dp} from radar observations is one of the most important issues involved in the K_{dp}-based QPE systems. However, being the range derivative of the propagation phase Φ_{dp}, K_{dp} cannot be easily estimated because of the noise, phase wrapping phenomenon, and associated fluctuation in the differential propagation phase. To resolve these problems, numerous algorithms have been proposed to estimate K_{dp} (e.g., [29], [30], [31], [32], [33]). Among them, the estimation approach developed by Wang and Chandrasekar [29] is implemented in the CASA QPE system. This estimation method will be described in more detail later in this chapter. For more information, one can also refer to the related literature [29].

3.1.2.3 Hybrid Algorithm

With the aid of dual-polarimetric observations, researchers often use more than one radar parameter to conduct rainfall estimations. In this thesis, rainfall algorithms based on more than one polarimetric radar parameter such as reflectivity (Z), differential reflectivity (Z_{dr}), and specific differential phase (K_{dp}) are all classified as hybrid algorithms. Several hybrid algorithms, including $R(Z, Z_{dr})$ and $R(Z_{dr}, K_{dp})$ based approaches, will be described in this section.

$R(Z, Z_{dr})$ Algorithm

Recall the definition of reflectivity factor (equation 3.11),

$$Z = \int_{D} D^{6} N(D) dD \tag{3.19}$$

For a gamma DSD model, Z/R can be expressed as [5],

$$Z/R = F(\mu)D_m^{2.33} \tag{3.20}$$

where $F(\mu)$ is a function depending on the gamma PDF parameter μ. It is shown that $F(\mu)$ varies very slowly with μ [34], and $D_m = a(Z_{dr})^b$, wherein a and b depend on the radar frequency bands [5]. Subsequently, the rainfall rate can be derived in the following form

$$R = \frac{a^{-2.33}}{F(\mu)} Z Z_{dr}^{-2.33b} \tag{3.21}$$

Equation 3.21 can be further refined as a simplistic estimator of the form

$$R = cZ^a Z_{dr}^b \tag{3.22}$$

It is worth mentioning that Z in the above equation often refers to horizontal polarization reflectivity (Z_h). Large errors can result from the measurement uncertainties involved in Z_{dr}, especially when mean Z_{dr} approaches 0 dB [5]. Gorgucci et al. have constructed a modified form [35] as below, which is more robust

$$R = a_1 Z^{b_1} 10^{0.1c_1 Z_{dr}} \tag{3.23}$$

A coefficient table (Table 3.2) was presented by Bringi and Chandrasekar by performing a non-linear regression analysis using the simulated R, Z and Z_{dr} data [5].

Table 3.2: Coefficients for usage of $R(Z, Z_{dr})$ algorithm at S-, C-, and X-bands.

Frequency Band	$\boldsymbol{a_1}$	$\boldsymbol{b_1}$	$\boldsymbol{c_1}$
S-band	6.7×10^{-3}	0.93	-3.43
C-band	5.8×10^{-3}	0.91	-2.09
X-band	3.9×10^{-3}	1.07	-5.97

$R(Z_{dr}, K_{dp})$ Algorithm

Recall equation 3.16,

$$K_{dp} \approx (\frac{180}{\lambda})10^{-3}CW(0.062D_m) \tag{3.24}$$

The water content W can be related to rainfall rate as [5]

$$\frac{W}{N_w} = \frac{F_3(\mu)}{[F_{3.67}(\mu)]^{4/4.67}}(\frac{R}{N_w})^{4/4.67} \tag{3.25}$$

where N_w (in mm^{-1}m^{-3}) is an "intercept" parameter defined as $N_w = \frac{2.67^4}{\pi\rho_\omega}(\frac{10^3 W}{D_0^4})$. In addition, based on the Beard-Chuang equilibrium shape relation [36], the mass-weighted mean diameter D_m can be expressed as

$$D_m = 1.619(Z_{dr})^{0.485} \tag{3.26}$$

wherein D_m is in mm and Z_{dr} is in dB.

Combining equations 3.24, 3.25, 3.26, we can obtain the $R(Z_{dr}, K_{dp})$ relation as

$$R(Z_{dr}, K_{dp}) = cZ_{dr}^a K_{dp}^b \tag{3.27}$$

However, this algorithm has large errors when Z_{dr} tends to 0 dB because of the negative value of b [5]. Gorgucci and Scarchilli proposed a more robust precipitation estimator using differential reflectivity and the specific differential phase [37] in the form,

$$R(Z_{dr}, K_{dp}) = a_2 10^{0.1 b_2 Z_{dr}} (K_{dp})^{c_2} \tag{3.28}$$

Similarly, a list of coefficients for different radar frequencies was given by Bringi and Chandrasekar by performing a non-linear regression analysis [5] (see Table 3.3).

Table 3.3: Coefficients for usage of $R(Z_{dr}, K_{dp})$ rainfall algorithm at S-, C-, and X-bands.

Frequency Band	$\boldsymbol{a_2}$	$\boldsymbol{b_2}$	$\boldsymbol{c_2}$
S-band	90.8	-1.69	0.93
C-band	37.9	-0.72	0.89
X-band	28.6	-1.37	0.95

However, in the actual applications, it is not easy to choose an optimal estimator for a given set of dual-polarimetric observations and/or a given type of rainfall since we need to determine which radar parameter can provide superior rainfall estimates (e.g., under which case can the phase term offer a better measurement relative to the other measurements such as Z and Z_{dr}?). Here, two hybrid algorithms will be briefly described. One is the radar rainfall relations developed at the National Severe Storms Laboratory (NSSL) during the Joint Polarization Experiment (JPOLE) designed to test the practicality and utility of a polarimetric WSR-88D radar, which will be referred to as the JPOLE-method. The other is the CSU-HIDRO algorithm developed by Cifelli et. al. [38]. For more details about these two approaches, one can refer to the related literature (for JPOLE-method see Ryzhkov et. al. [39] and for CSU-HIDRO, see Cifelli et. al. [38].

JPOLE-Method

In the JPOLE-method, the value of the rain rate given by the following standard Weather Surveillance Radar-1988 Doppler (WSR-88D) R(Z) relation will be used for selecting the rainfall rate expressions:

$$Z = 300R^{1.4} \tag{3.29}$$

where Z is expressed in $\mathrm{mm}^6\mathrm{m}^{-3}$ and R in mm hr^{-1} and the magnitude of Z is limited to a maximum of 53dBZ to mitigate hail contamination. The dual-polarimetric rainfall rate is estimated based on the $R(Z)$ values. If $R(Z) < 6\mathrm{mm\ hr}^{-1}$, then

$$R = R(Z)/(0.4 + 5.0|Z_{dr} - 1|^{1.3}) \tag{3.30}$$

If $50 > R(Z) > 6\mathrm{mm\ hr}^{-1}$, then

$$R = R(K_{dp})/(0.4 + 3.5|Z_{dr} - 1|^{1.7}) \tag{3.31}$$

If $R(Z) > 50\mathrm{mm\ hr}^{-1}$, then $R = R(K_{dp})$, where

$$R(K_{dp}) = 44.0|K_{dp}|^{0.822} sign(K_{dp}) \tag{3.32}$$

where Z_{dr} is the differential reflectivity in a linear scale and K_{dp} is in degree/km.

CSU-HIDRO Algorithm

The CSU-HIDRO algorithm was based on the hydrometeor identification (HID) results, namely, rain, mixture, or ice. A fuzzy logic technique-based hydrometeor classification system was developed by Lim et. al [40] that was implemented in the CSU-HIDRO algorithm to guide the rainfall application. The advantage of this hydrometeor classification method [40] is to use both additive and product rules in inference for balancing the metrics of probability error and false positive classification. The weight factor was also used according to hydrometeor types and radar variables, which means that we can use the observations more effectively to identify precipitation types, taking their error structure into account. The logic of CSU-HIDRO is shown as Figure 3.1. The rainfall estimation relations used in the CSU-HIDRO algorithm corresponding to the flowchart in Figure 3.1 are

$$R(K_{dp}) = 40.5K_{dp}^{0.85} \tag{3.33}$$

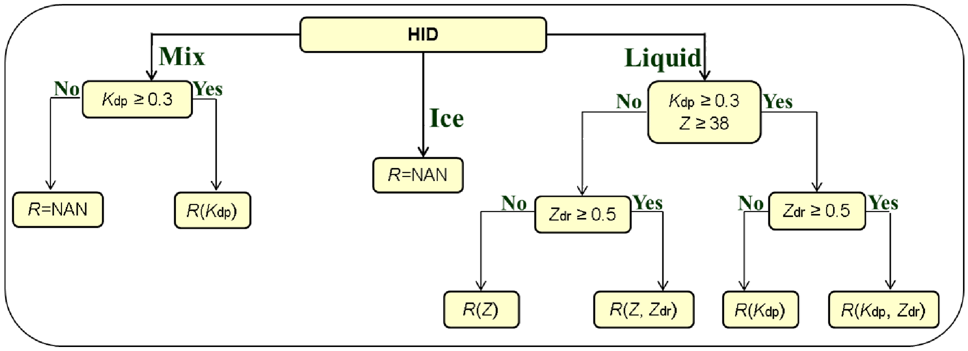

Figure 3.1: Logic of CSU-HIDRO algorithm.

$$R(Z) = 0.017Z^{0.7143} \tag{3.34}$$

$$R(Z, Z_{dr}) = 6.7 \times 10^{-3} Z^{0.927} 10^{(-0.343 Z_{dr})} \tag{3.35}$$

$$R(K_{dp}, Z_{dr}) = 90.8 K_{dp}^{0.93} 10^{(-0.169 Z_{dr})} \tag{3.36}$$

Using the data from CSU-CHILL radar and a rain gauge network, the authors showed the new HID-based algorithm could provide good performance for rainfall events in Colorado.

3.2 CASA QPE Methodology

The CASA's DCAS network maintains a system "heartbeat" of about 30s. After finishing two low-level full 360-degree scans, CASA radars conduct adaptive scans at different elevations depending on the location of the precipitation echoes to collect accurate observations. The measured specific differential propagation phase (K_{dp}) will be used for QPE processing since K_{dp} is less sensitive to drop size distribution compared with other terms such as Z and Z_{dr}. It is also relatively less prone to calibration errors and path attenuation. Generally, the accuracy of radar QPE relies both on the radar system such as beamwidth and sidelobe, and on environmental factors such as clutter and storm variability [47]. Radar observations of precipitations can also be contaminated by hail, melting hydrometeor particles, and/or ground clutter. Especially in urban environments, strong clutters are expected from scattering of buildings, which are "perfect" reflectors when radar is steered down low. In addition, radar calibration errors and anomalous propagation can pollute radar rainfall estimations. Saltikoff et al. summarized the factors leading to the quality assurance of weather radar data for QPE from a network prospective [41]. In this section, various sensing aspects of the CASA DCAS system design for QPE will be briefly presented, including spatial and temporal resolution, sensitivity, beam height, estimation of K_{dp}, and rainfall algorithm description.

3.2.1 Spatial Resolution

Maki et al. have developed a high-resolution hydrologic model on the order of tens of meters for urban flood monitoring and mitigation [42], which is a very good example of a CASA application. Radar rainfall measurements of commensurate resolution are needed to achieve its full capability. In addition, beam broadening can affect the quality of dual-polarization radar measurements in the presence of non-uniform beam filling [43] [44]. The spatial resolution is determined by the beamwidth, system bandwidth, and radar slant range. For longer ranges, the transmitted beam will extend a wider distance across beam, which can result in substantial biases. Currently, the National Weather Service Weather Surveillance Radar network (NEXRAD) provides radar data at the maximum NEXRAD range/radius of about 230 km, or 150 km in super-resolution mode. This corresponds to a cross-beam distance larger than 5 km at 300 km range, virtually preventing reliable quantitative rainfall estimates either in vertical or in horizontal direction. The cross-beam distance will be scaled down to 700 meters when the range is limited within 40 km, which will result in finer QPE grids. The CASA DCAS system is able to achieve great cross-beam resolution using a group of short-range X-band dual polarization radars with a maximum range of about 40 km and beam width of approximately 1.8 degrees to produce a mean cross-beam less than 750 m. Along the radial range, the radars have a range resolution of better than 100 m. In the overlapping areas of different radars, we can choose the smaller resolution samples. Junyent and Chandrasekar [45] presented a detailed analysis of the sampling volume resolution as a function of beam width, network topology and degree of overlap for CASA Integrated Project 1 (IP1) network.

3.2.2 Temporal Resolution

To evaluate the quick response of fast-moving and/or evolving urban rainfall events, high temporal resolution real-time rainfall product generation is required. The NEXRAD network renders observations with updates every five to six minutes across the United States. However, much can happen within five to six minutes! A short sampling interval is particularly valuable in extreme rain storms since it may only takes tens of minutes for an urban basin to reach its peak discharge from dry conditions. As flood monitoring pinpoints down to specific blocks, the temporal variability is even higher and a sampling at five to six minutes can miss the local peaks. In the CASA radar system, the system update time is of the order of 60 seconds due to the implementation of an adaptive, coordinated sector scanning strategy. Such temporal resolution is very important for the monitoring and mitigation of urban flash floods, where the watersheds can respond quickly. The DCAS system can also automatically and adaptively change its scan patterns to correspond to detected atmospheric conditions and user preferences. The CASA scan strategy systems are described by Zink et al. [46].

3.2.3 Clutter Mitigation

Ground clutter can often lead to misinterpretation of radar observations, which may result in inappropriate actions within the closed-loop system. The radar reflectivity for clutter echo can be expressed as [47],

$$Z_{ec} < dBZ >= 2f(\alpha) + \sigma^0 < dB > + C_0 + 10 \log_{10} \frac{A_c < km^2 >}{V_c < km^3 >} \tag{3.37}$$

where $f(\alpha)$ is the sidelobe pattern at clutter incidence angle, σ^0 is the surface backscattering coefficient, C_0 is the radar constant, A_c is the beam illuminated area, and V_c is the effective radar resolution volume. At low grazing angles, A_c is proportional to range. Reflection from buildings and other close architectures often have a high grazing angle, A_c will be independent of range, and σ^0 can be larger by several orders under these circumstances. Substantial beam blockages will result when those buildings and/or architectures intercept the mainlobe. Chandrasekar et al. proposed a high-performance parametric clutter filter using advanced spectral approaches (Gaussian Model Adaptive Processing, GMAP [48]), which was implemented in CASA IP1 test bed [49]. In this clutter filtering approach, clutter spectral coefficients were notched with a spectral filter based on a Gaussian model for the clutter spectral density. A Gaussian weather spectral density is recursively fit to the remaining points and the notched spectral coefficients are interpolated and the bias in reflectivity and velocity due to notch filtering is minimized. In addition, use of small-size radar enables flexible deployment so that clutter can be effectively reduced by more choice of installation sites. For example, rooftop installation on tall buildings can be used in an urban environment. It should be mentioned here that clutter filtering of dual-polarization signals is rather important because CASA QPE is K_{dp}-based. As a result, the effect of clutter will be eliminated in the CASA QPE system when combining the networked radar application and advanced clutter filtering.

3.2.4 Beam Height Analysis

The radar observations and rainfall measurements will be close to the ground if the radar scanning angle is lower, which is one of the determining factors of beam heights. However, to avoid QPE biases, the radar beam should be above the significant mainlobe clutters such as high buildings while containing the atmospheric conditions below bright bands or melting layers [44]. In addition, the earth's curvature and blockage by the local terrain can prevent the coverage of raining regions of interest. At long ranges, the beam height can be very high because of the earth's curvature, in which case the lower atmosphere will not be able to be detected. For instance, at the maximum range of NEXRAD (about 230 km), the beam height is higher than 3 km at 0° scanning elevation angle. What is more, current regulations limit the lowest elevation angle used by NEXRAD to 0.5°. Figure 3.2 shows the beam height as a function of the range from the radar using the 4/3 earth curvature model. It can be seen that 1 km height observation can be achieved

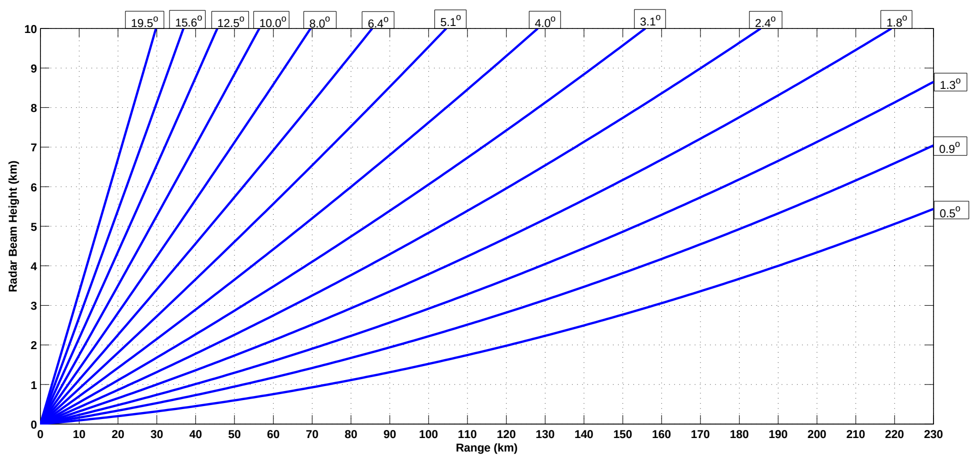

Figure 3.2: Beam height vs. radar range at the elevation angles corresponding to one of the scan strategies of WSR-88D (VCP-12).

at 1° elevation angle if the maximum range is limited to 50 km. This is another major advantage of using a dense short-range radar network for precipitation measurement [45]. It is also important to avoid clutter contamination when we choose lower beam height for better radar QPE.

3.2.5 Sensitivity

Sensitivity is another important parameter that needs to be evaluated since it can reflect minimal detectable rainfall. The sensitivity of meteorological radar is proportional to the transmit power and inversely related to the square of the radar range, as shown below [5],

$$Ze_{min} = SNR_0 N_0 \frac{2^{10}(ln2)\lambda^2 10^{18}}{G_a^2|K_w|^2\pi^3 c\tau\theta_h\theta_v} r^2\alpha^2 \frac{1}{P_t} \tag{3.38}$$

where SNR_0 is the minimal signal-to-noise ratio, N_0 is the system noise floor, r is radar range, G_a is antenna gain, τ is pulse duration, α is system loss, θ_h and θ_v are beamwidth, and P_t denotes the transmitted power.

Obviously, the use of small, short-range X-band radars can greatly relax the sensitivity constraints compared with the large S-, or C-band radars. The CASA DCAS radar network can further improve the system's reliability because it has large overlapping coverage (i.e., multiple propagation paths exist from different radars to a common volume). However, for X-band radar systems like CASA radars, an extra margin needs to be allocated for the transmitted power because of the significant rain attenuation at X-band frequencies. This attenuation margin is also range dependent and it is more likely to be higher at longer propagation ranges. Chandrasekar et al. have shown that the attenuation margin needed for X-band radars is about 12 dB for the South Central United States such as the Oklahoma and Texas region [50], but this attenuation margin can change with different synoptic characteristics.

3.2.6 Estimation of Specific Differential Propagation Phase

As mentioned in section 3.1.2.2, the estimation of K_{dp} is not an easy task due to measurement noise, unreliability in lighter rainfall, and artifacts stemming from the non-uniform beam filling effect. By definition, the specific differential phase (K_{dp}) between two horizontally and vertically polarized 'characteristic' waves is [5],

$$K_{dp} = -10^3\Im(\lambda_1 - \lambda_2) = 10^3(\frac{2\pi n}{k_0})\Re[\widehat{h}\cdot\overrightarrow{f}(\widehat{i},\widehat{i}) - \widehat{v}\cdot\overrightarrow{f}(\widehat{i},\widehat{i})] \tag{3.39}$$

where $\Im(*)$ and $\Re(*)$ are the imaginary and real parts of the complex number $(*)$, respectively. λ_1 and λ_2 are eigenvalues of the horizontally and vertically polarized waves. $\overrightarrow{f}(\widehat{i},\widehat{i})$ is the forward scattered vector amplitude and n is the number of the spheres per unit volume.

The specific differential phase can be estimated as the range derivative of the propagation phase Φ_{dp},

$$K_{dp} = [\Phi_{dp}(r_2) - \Phi_{dp}(r_1)]/[2(r_2 - r_1)] \tag{3.40}$$

Nevertheless, radar does not measure the forward propagation phase Φ_{dp} directly. Usually, the total differential phase Ψ_{dp} can be estimated from co-polar covariance that consists of both the phase shifts resulting from forward propagation and backscattering. As shown in Bringi and Chandrasekar (2001) [5], the differential phase between co-polar signals, Ψ_{dp}, can be expressed as

$$\Psi_{dp} = \arg[(V_h^{10})^*(V_v^{01})] = \arg[\exp^{2(\lambda_2-\lambda_1)r}] + arg(S_{hh}^* S_{vv})_{BSA} \tag{3.41}$$

where V_h^{10} and V_v^{01} are the voltages at the h-port and v-port, respectively. S_{hh}^* and S_{vv} are components of the scattering matrix [5]. Equation 3.41 can also be written as

$$\Psi_{dp} = \Phi_{dp} + \delta_{co} \tag{3.42}$$

where Φ_{dp} is the 2-way differential propagation phase (often called differential propagation phase), and δ_{co} is the back scatter differential phase.

But accurate K_{dp} estimates can only be obtained if δ_{co} is constant or negligible along the range gate or δ_{co} can be correctly measured separately. Usually, the total differential phase can be processed for K_{dp} estimation. Range filtering of Ψ_{dp} profiles is commonly employed to separate Φ_{dp} signals from unwanted components such as environmental and system noise and δ_{co}. Unfortunately, we still do not have a standard processing or universally adopted method to accurately measure K_{dp} within the radar community even though numerous algorithms have been proposed in the last two decades to tackle challenges associated with the aforementioned issues. These algorithms can be classified into two types. In one, the K_{dp} estimates are purely based on Ψ_{dp} measurements, and the other type uses auxiliary data such as reflectivity and/or the differential reflectivity and the self-consistency relations between polarimetric observables in order to obtain a more accurate estimate of K_{dp} or δ_{co}. Assuming any existing method as interchangeable may lead to large errors for subsequent processing for issues like hydrological applications and flood warning. The challenges are exacerbated at shorter wavelengths, wherein the expectation for an increased total differential phase shift (Ψ_{dp}) through similar rain conditions can be compromised by significant contributions from a nonzero differential backscatter phase shift.

In the K_{dp}-based CASA QPE system, the adaptive estimation method proposed by Wang and Chandrasekar is implemented to suppress noise fluctuations and reduce estimation errors [29]. The adaptive estimation is tuned to local variability and statistical fluctuation and performed in the complex domain. For computation of rainfall rate, only K_{dp} from the 2° elevation angle is used since the 2° elevation scan is the surveillance scan in CASA's DCAS scan strategy. At the 2° elevation angle, the impact of sidelobe clutter will be minimal after clutter filtering. All of the synchronized scans are merged onto latitude-longitude grids for further processing and usage. That is, the K_{dp} field from all the radar notes are fused before the rainfall conversion is applied. Especially in the overlapping area of CASA radars, the "signal" loss resulting from rain attenuation is compensated and the K_{dp}s from different radars are merged based on the quality of the individual K_{dp}. The main factor determining the data quality is the range that represents the lowest beam height because the scanning elevation for all radars is fixed as 2°. Overall, the data fusion K_{dp} can improve the rainfall application. However, this is not always the best solution for the X-band radar network since the path attenuations from different directions are different.

Figure 3.3 is an example showing the K_{dp} from each individual radar and the merged K_{dp} for rainfall estimation.

3.2.7 CASA Dual-polarization Radar Rainfall Algorithm Description

Recall the relation between drop size distribution and the instantaneous still-air rainfall rate (equation 3.12) and the expression of specific differential propagation phase (K_{dp}) through DSD [5]:

$$R = 0.6\pi \times 10^{-3} \int v(D) D^3 N(D) dD \tag{3.43}$$

$$K_{dp} = \frac{\pi^2}{6\lambda} C \int (1 - r) D^3 N(D) dD \tag{3.44}$$

Again, C is a constant, r is the axis ratio of raindrops, and λ is the wavelength.

Obviously, both R and K_{dp} can be approximated as moments of DSD. Thus the $R(K_{dp})$ relation can be expressed in a power-law form as mentioned in above equation 3.17,

$$R(K_{dp}) = a K_{dp}^b \tag{3.45}$$

For the CASA dual-polarization X-band radars at about 9.4 GHz in the IP1 test bed in Southwestern Oklahoma, the above relation is scaled to [47],

$$R = 18.15 K_{dp}^{0.791} \tag{3.46}$$

which is used for rainfall estimation.

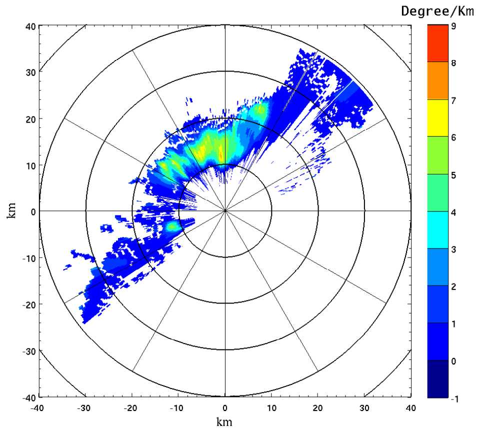

(a) KCYR

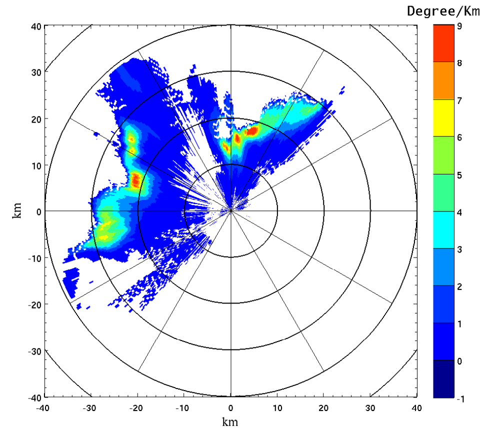

(b) KSAO

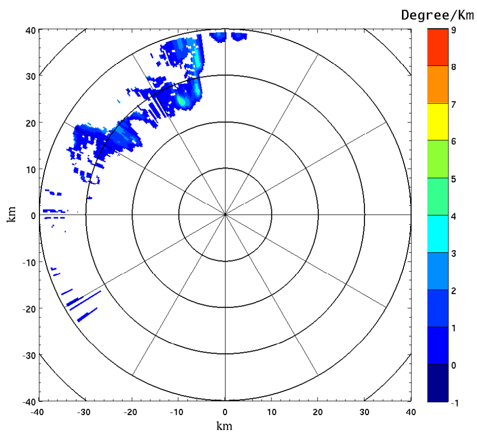

(c) KLWE

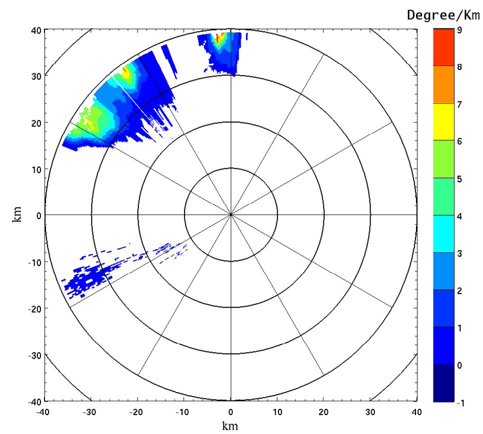

(d) KRSP

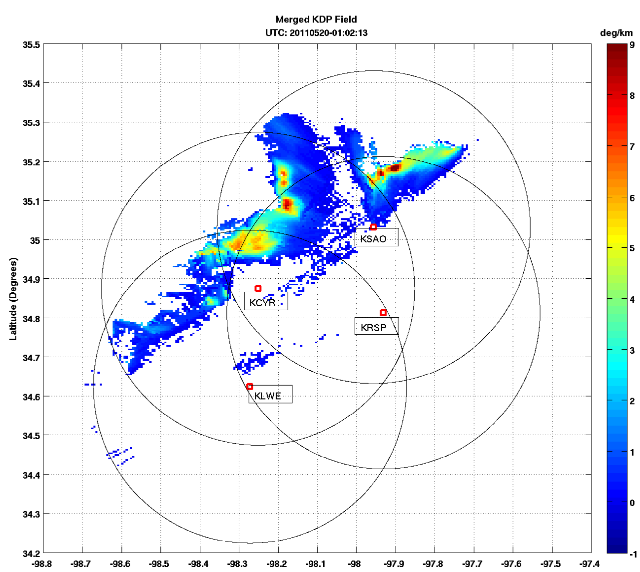

(e) Merged Result

Figure 3.3: Estimated K_{dp} from individual IP1 radars and corresponding merged results at 01:02UTC on May 20, 2011.

3.3 Ground Validation for CASA QPE System

Without loss of generality, CASA is using the surface rainfall measurements from ground rain gauges as validation and assessment tools. A U.S. Department of Agriculture Agricultural Research Service's (ARS) gauge network (Micronet) in the Little Washita River Experimental Watershed (LWREW) is used for the evaluation purposes. The ARS Micronet is operated and maintained by the Agricultural Research Service's Grazinglands Research Laboratory in cooperation with Oklahoma State University and the Oklahoma Climatological Survey. Meteorological and hydrologic conditions in LWREW have been measured since 1961 (information on line at $http://ars.mesonet.org$). The LWREW consists of 20 rain gauge stations comprising an area of about 611 km^2 that covers parts of Caddo, Comanche, and Grady counties. It is right in the center of CASA's IP1 test bed (see Figure 3.4). The location informations for these 20 rain gauges can be found in table 3.4.

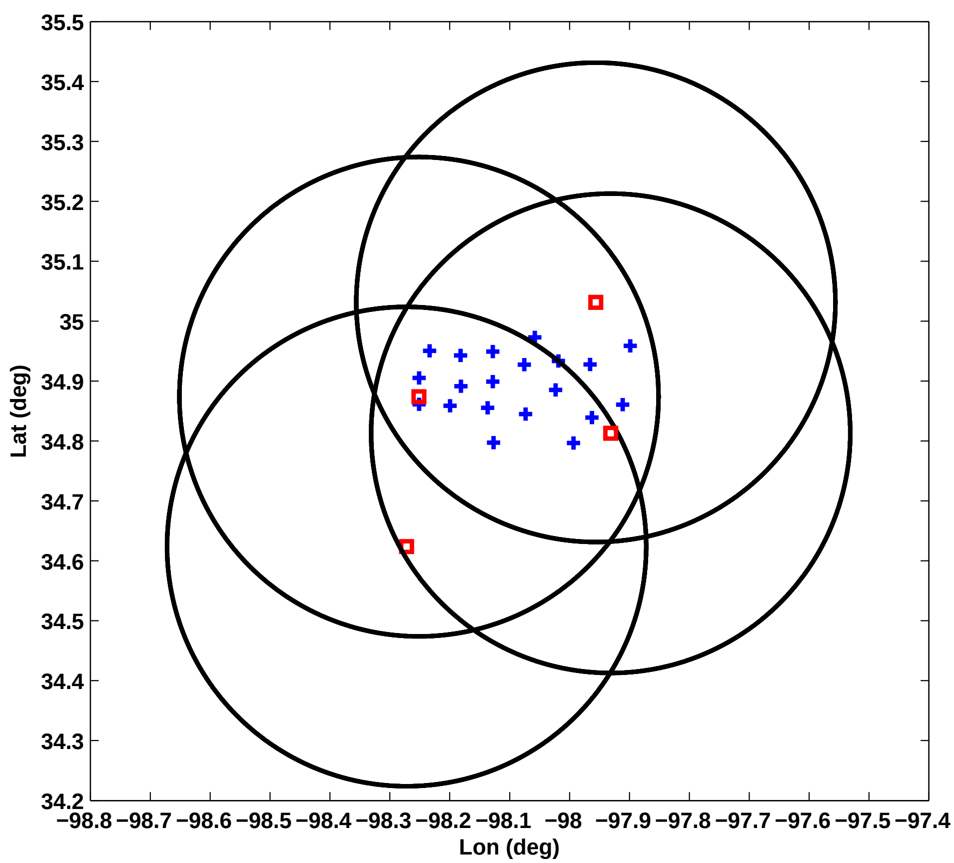

Figure 3.4: Locations of USDA ground gauges (blue cross) in CASA's IP1 network.

Table 3.4: 20 rain gauges used for cross-validating radar QPE.

Station Name	**Latitude (deg.)**	**Longitude (deg.)**	**Elevation(inch)**
ARS Site 121	34.958600	-97.898600	343
ARS Site 124	34.972800	-98.058100	387
ARS Site 131	34.950300	-98.233600	458
ARS Site 132	34.942800	-98.181900	456
ARS Site 133	34.949200	-98.128100	430
ARS Site 136	34.927800	-97.965600	343
ARS Site 146	34.885300	-98.023100	358
ARS Site 148	34.899200	-98.128100	431
ARS Site 152	34.861100	-98.251100	416
ARS Site 154	34.855300	-98.136900	393
ARS Site 159	34.796700	-97.993300	439
ARS Site 234	34.927445	-98.075452	399
ARS Site 235	34.933460	-98.018777	372
ARS Site 244	34.860714	-97.911140	401
ARS Site 249	34.891386	-98.181246	404
ARS Site 250	34.905249	-98.251060	345
ARS Site 253	34.858720	-98.199458	413
ARS Site 256	34.838957	-97.962534	363
ARS Site 262	34.797347	-98.126933	423
ARS Site 282	34.845039	-98.073473	376

The rainfall measurements collected by the 20 gauges are archived as accumulations at five-minute intervals over every 24-hour period in local time (Central Standard Time) with a resolution of about 0.254 mm. As shown in the following screen-shot of a data file (see figure 3.5), every archived file has a line each for the "version" string, station ID, and the date, followed by a header line and all recorded data. Table 3.5 is an explanation of each column parameter header in the archived files. Every observed parameter is followed by a column of data with a header that starts with "Q", which indicating the quality check (QC) character: g stands for "good" (passed QC tests - extremely low probability of error); S stands for "suspect" (QC tests indicate some suspicion - low probability of error); W stands for "warning" (several QC test failures - high probability of error); F stands for "failure" (known error); M stands for "missing" (data not received); I stands for "ignore"; N stands for "not installed"; and U stands for "unknown". More information about the climate data can be found on line at $http : //ars.mesonet.org/about_data/documentation.php$. For better validation, the radar estimates are spatially chosen at the location of each rain gauge, whereas the rain gauge estimates are temporally interpolated at the scan time of the radar network (i.e., one minute).

Similarly, a rain gauge network in the DFW urban demonstration network will serve as the ground validation tool to demonstrate CASA QPE in the urban environments. The gauge network includes a

```
version: a5m122
station: A136
date   : 2007-05-07

 STID  TIME     RAIN Q   RELH Q   TAIR Q   SRAD Q   TS05 Q   TS10 Q   TS15 Q   TS30 Q   BATV   FLSV    VW05 Q    VW25 Q    VW45 Q   SKIN Q
 A136  00 05    0.00 g   81.9 g   23.8 g    0.0 g   -995 I   -995 I   -995 I   -995 I   13.0   -996    -995 I    -995 I    -995 I   20.5 g
 A136  00 10    0.00 g   81.2 g   23.9 g    0.0 g   -995 I   -995 I   -995 I   -995 I   13.0   -996    -995 I    -995 I    -995 I   20.6 g
 A136  00 15    0.00 g   80.7 g   24.0 g    0.0 g   21.2 W   21.6 g   21.1 g   20.1 g   13.0   -996    -995 I    -995 I    -995 I   20.7 g
 A136  00 20    0.00 g   80.5 g   24.0 g    0.0 g   -995 I   -995 I   -995 I   -995 I   13.0   -996    -995 I    -995 I    -995 I   20.7 g
 A136  00 25    0.51 g   82.4 g   23.9 g    0.0 g   -995 I   -995 I   -995 I   -995 I   13.0   -996    -995 I    -995 I    -995 I   20.2 g
 A136  00 30    0.51 g   85.1 g   23.4 g    0.0 g   21.2 W   21.5 g   21.1 g   20.1 g   13.0   -996    0.14 g    0.11 g    0.15 g   19.7 g
 A136  00 35    0.51 g   85.8 g   23.2 g    0.0 g   -995 I   -995 I   -995 I   -995 I   13.0   -996    -995 I    -995 I    -995 I   19.6 g
 A136  00 40    0.76 g   85.1 g   23.3 g    0.0 g   -995 I   -995 I   -995 I   -995 I   13.0   -996    -995 I    -995 I    -995 I   19.7 g
 A136  00 45    0.76 g   86.0 g   23.3 g    0.0 g   21.1 W   21.5 g   21.1 g   20.1 g   13.0   -996    -995 I    -995 I    -995 I   19.6 g
 A136  00 50    0.76 g   87.0 g   23.1 g    0.0 g   -995 I   -995 I   -995 I   -995 I   13.0   -996    -995 I    -995 I    -995 I   19.7 g
 A136  00 55    4.57 g   88.1 g   23.0 g    0.0 g   -995 I   -995 I   -995 I   -995 I   13.0   -996    -995 I    -995 I    -995 I   19.6 g
 A136  01 00   10.16 g   91.9 g   22.4 g    0.0 g   21.1 W   21.5 g   21.0 g   20.1 g   13.0   -996    0.14 g    0.11 g    0.14 g   19.6 g
 A136  01 05   11.43 g   90.0 g   21.1 g    0.0 g   -995 I   -995 I   -995 I   -995 I   13.0   -996    -995 I    -995 I    -995 I   18.5 g
 A136  01 10   11.43 g   91.6 g   20.2 g    0.0 g   -995 I   -995 I   -995 I   -995 I   13.0   -996    -995 I    -995 I    -995 I   18.0 g
 A136  01 15   11.68 g   86.8 g   19.4 g    0.0 g   21.1 W   21.5 g   21.0 g   20.1 g   13.0   -996    -995 I    -995 I    -995 I   16.9 g
 A136  01 20   11.68 g   87.1 g   18.8 g    0.0 g   -995 I   -995 I   -995 I   -995 I   13.0   -996    -995 I    -995 I    -995 I   16.3 g
```

Figure 3.5: A screen shot of a sample gauge data file.

Table 3.5: Header information of rain gauge data files.

Header Name	Meaning	Header Name	Meaning
STID	station ID	**TS25**	soil temperature at 25 cm depth (deg C)
TIME	CST time (hr min.)	**TS30**	soil temperature at 30 cm depth (deg C)
RAIN	rainfall since 00 UTC (mm)	**TS45**	soil temperature at 45 cm depth (deg C)
RELH	relative humidity at 1.5 m (%)	**BATV**	battery voltage (volts)
TAIR	air temperature at 1.5 m (deg C)	**FLSV**	flag status value
SRAD	solar radiation (W/m^2)	**VW05**	soil volumetric water at 05 cm depth (water fraction by volume)
TS05	soil temperature at 05 cm depth (deg C)	**VW25**	soil volumetric water at 25 cm depth (water fraction by volume)
TS10	soil temperature at 10 cm depth (deg C)	**VW45**	soil volumetric water at 45 cm depth (water fraction by volume)
TS15	soil temperature at 15 cm depth (deg C)	**SKIN**	skin temperature (deg C)

number of U.S. Geological Survey (USGS) gauges and 25 stream gauges that are part of the High Water Warning System Sites in the City of Fort Worth, Texas. Figure 3.6 shows the locations of the 25 gauges relative to the radar umbrellas.

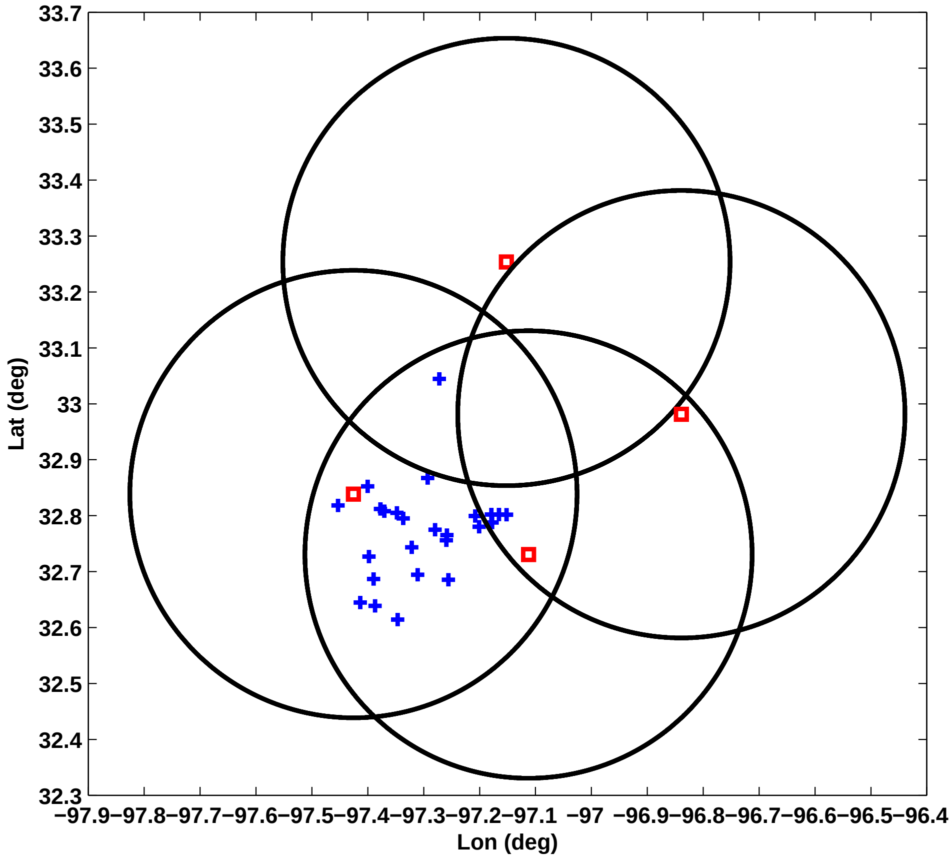

Figure 3.6: Locations of 25 stream gauges (blue crosses) in DFW urban network

3.4 Error Analysis

Radar QPE is not a simple process. It involves issues both from the physically based inferences and the engineering aspect. The elements that need to be considered include hardware design, signal processing, electromagnetic wave propagation through the precipitations, microphysics of clouds and precipitation, quality control, and following hydrologic applications. Rainfall estimation errors can occur in sub-modules such as radar calibration techniques, improper rainfall relationships, and sub-cloud evaporation of raindrops. All will lead to departures of estimated rainfall from true rainfall. Identifying and quantifying those various biases are among the most important steps in characterizing the uncertainties of radar QPE. Using dual-polarization techniques, radar rainfall estimation can be improved with additional radar measurements such as K_{dp} and Z_{dr}. In addition, the polarimetric measurements provide more information for classifying precipitation types (rain, hail, graupel, and/or snow) and distinguishing the ground echo due to local clutter and anomalous propagation conditions from precipitation. How to eliminate the various error sources is beyond the focus of this thesis. However, to quantify the errors of the CASA QPE system, the mean bias, normalized mean bias, and the normalized standard error (NSE) are defined as follows, using the gauge observations as the baseline for cross-comparison:

$$< e >=< R_R - R_G > \tag{3.47}$$

$$< e >_N = \frac{< R_R - R_G >}{R_G} \tag{3.48}$$

$$NSE = \frac{< |R_R - R_G| >}{R_G} \tag{3.49}$$

where the angle brackets denote the sample average, and R_R and R_G represent instantaneous rainfall rate or rainfall accumulation estimated from radar and gauge, respectively.

The evaluation results will be presented in Chapter 4.

3.5 Summary

This chapter has presented an extensive description of different radar parameter-based quantitative precipitation estimation (QPE) algorithms, starting with a brief review of commonly used raindrop size distribution (DSD) models. The CASA QPE methodologies were then focused on. Considerations for implementation of CASA QPE, including analysis of spatial and temporal resolution, clutter mitigation, beam height, and sensitivity were given. The adaptive estimation of specific differential propagation phase and CASA dual-polarization rainfall algorithm were also presented. A detailed description of the gauge network used for ground validation and evaluation of CASA QPE was then provided, including the gauge management and locations, data format and processing, and the definition of the performance evaluation metrics. The CASA QPE products and performance evaluation results will be presented in the next chapter.

CHAPTER 4

EXPERIMENTS AND RESULTS

4.1 5-year Validation of CASA IP1 Experiments

Since the deployment of the CASA IP1 radar network in 2006, numerous experiments have been conducted to demonstrate and evaluate the DCAS concepts. In the storm seasons from 2007 to 2011, tens of rainfall events were observed passing over the radar coverage and Little Washita Experimental Watershed [47] [52]. In this thesis, about 174.4 hours of data from 40 precipitation events are used for performance evaluation and cross-comparisons, which include singlecells, multicells and supercells. The cross-comparison pairs were chosen at each rain gauge station for each precipitation event. Table 4.1 summarizes the rainfall cases during the past five-years' operations.

Table 4.1: 40 rainfall events to be analyzed.

Date	**Rough Time (UTC)**	**Duration ($\approx$ hr)**	**Date**	**Rough Time (UTC)**	**Duration ($\approx$ hr)**
2007-05-07	06:10-13:40	7.5	2009-05-05	15:00-17:40	2.7
2007-05-08	07:00-10:40	3.7	2009-05-11	09:40-15:00	5.3
2007-05-10	22:20-24:00	1.7	2009-05-14	03:00-07:00	4.0
2007-06-10	22:50-24:00	1.2	2009-05-16	02:50-08:20	5.5
2007-06-11	00:00-01:00	1.0	2009-06-02	06:20-07:30 18:00-19:30	2.7
2007-06-14	06:40-11:00	4.3	2009-06-03	05:40-09:40	4.0
2007-06-20	05:00-11:40	6.7	2009-06-15	07:40-09:00	1.3
2008-05-27	08:00-10:30	2.5	2010-01-28	11:40-22:00	10.3
2008-06-06	02:20-04:40	2.3	2010-03-20	06:40-08:20	1.7
2008-06-09	08:40-20:00	11.3	2010-04-02	10:40-13:40	3.0
2008-06-17	06:20-07:30 14:00-18:00	5.2	2010-05-13	08:00-10:40	2.7
2008-06-19	08:00-10:30	2.5	2010-06-14	18:00-23:20	5.3
2008-10-06	07:20-11:40	4.3	2010-06-15	02:00-07:40	5.7
2009-02-09	09:00-12:00	3.0	2010-09-08	09:40-24:00	14.3
2009-02-10	23:00-24:00	1.0	2010-09-09	00:00-03:00	3.0
2009-03-24	01:40-03:20	1.7	2011-02-24	13:00-16:20	3.3
2009-03-27	18:20-24:00	5.7	2011-04-24	18:20-21:40	3.3
2009-04-27	02:00-04:40	2.7	2011-05-01	12:30-16:40	4.2
2009-04-29	10:00-15:20	5.3	2011-05-11	16:40-22:00	5.3
2009-05-02	09:00-15:40	6.7	2011-05-20	03:00-05:00 09:30-14:00	6.5
Total Observations: about 174.4 hours					

4.2 Sample Real-time Products and Performance Evaluation Results

4.2.1 Sample Products from CASA QPE System

Normally, the CASA QPE system produces three types of high spatial and temporal resolution rainfall products updated at every minute, namely, instantaneous rainfall rate map, hourly rainfall measurement map, and point-wise diagnostic traces for 5-, 10-, 15-, 20-, 30- and 60-minute (hourly) rainfall estimates. These products were selected according to the system operation requirements and end users' feedback, especially for flash flood monitoring and mitigation applications. It should be noted that the extent of averaging can be adjusted to match the response scale of the watershed of interest. For the IP-1 test bed in southwestern Oklahoma, this time was set at 60 minutes. The following maps (Figure 4.1 to Figure 4.6) are some examples of instantaneous rainfall rate and hourly rainfall accumulation maps at CASA IP1 testbed for several storm events. Figure 4.7 to Figure 4.11 are sample products of the estimated point-wise traces at some gauge locations for several rainfall events during the storm experiments. The detailed point-wise traces are used for diagnostic purposes for comparison against rain gauges in the Little Washita River Experimental Watershed (LWREW).

From the high-resolution products from the CASA QPE system, we can see the great potential of the networked X-band radar QPE for use in downstream applications such as input to hydrological and hydraulic models, and further forecasting and mitigation of floods.

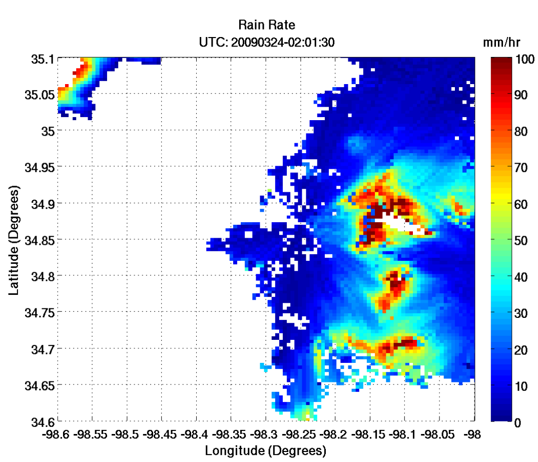

(a) rainfall rate map

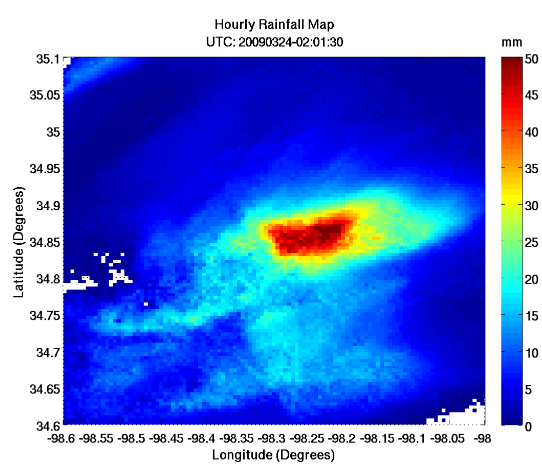

(b) hourly rainfall map

Figure 4.1: Sample products of regional rainfall map for March 24, 2009, storm event (UTC: 02:01:30).

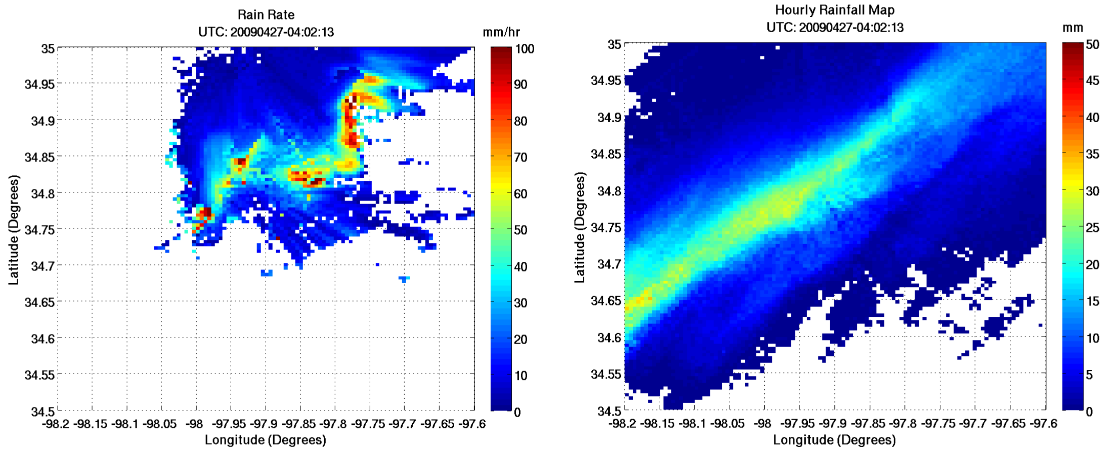

(a) rainfall rate map

(b) hourly rainfall map

Figure 4.2: Sample products of regional rainfall map for April 27, 2009, storm event (UTC: 04:02:13).

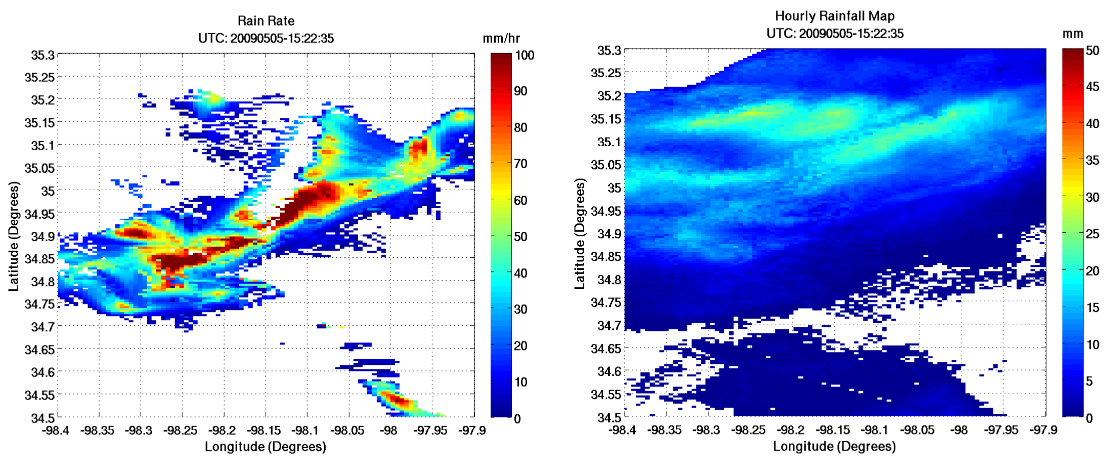

(a) rainfall rate map

(b) hourly rainfall map

Figure 4.3: Sample products of regional rainfall map for May 05, 2009, storm event (UTC: 15:22:35).

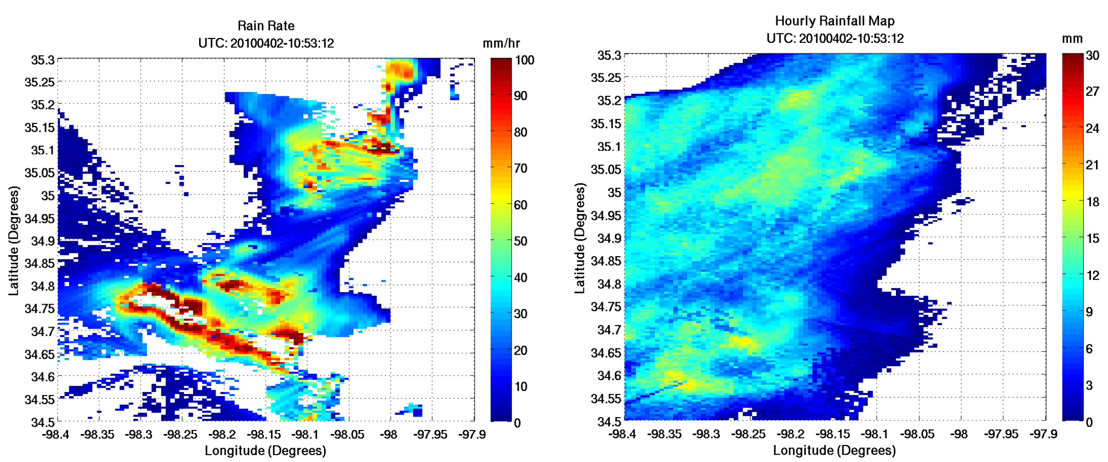

(a) rainfall rate map

(b) hourly rainfall map

Figure 4.4: Sample products of regional rainfall map for April 02, 2010, storm event (UTC: 10:53:12).

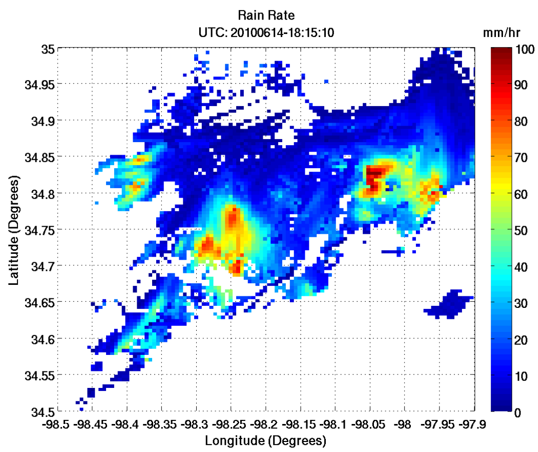

(a) rainfall rate map

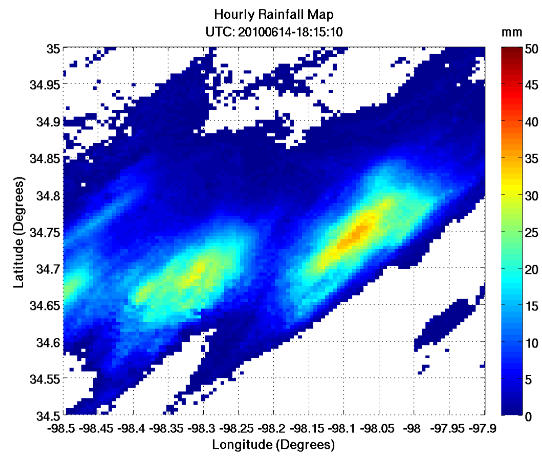

(b) hourly rainfall map

Figure 4.5: Sample products of regional rainfall map for June 14, 2010, storm event (UTC: 18:15:10)

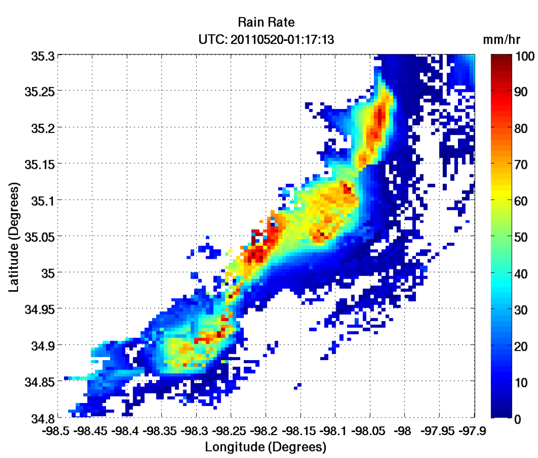

(a) rainfall rate map

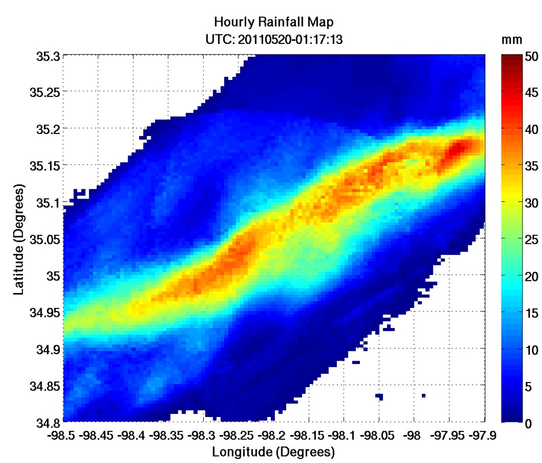

(b) hourly rainfall map

Figure 4.6: Sample products of regional rainfall map for May 20, 2011, storm event (UTC: 01:17:13).

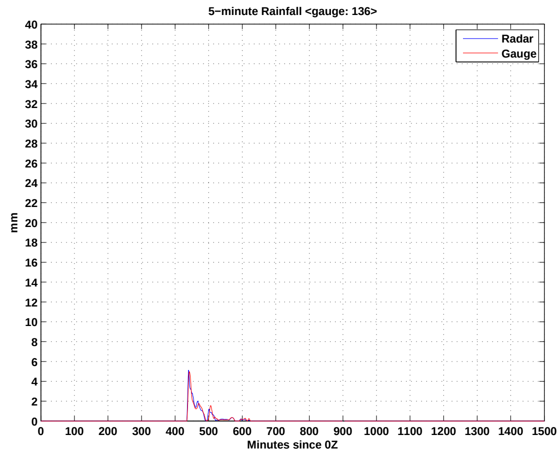

(a) 5-min rainfall point-wise trace

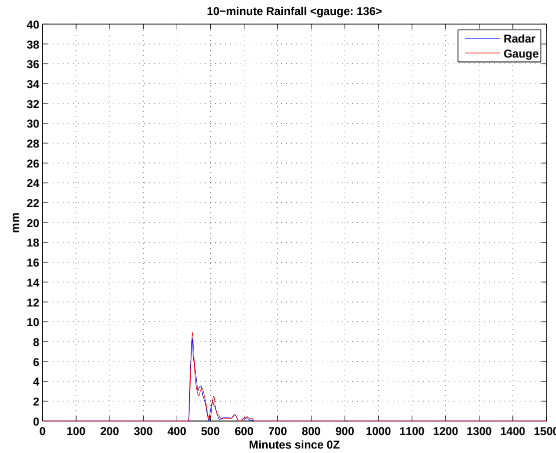

(b) 10-min rainfall point-wise trace

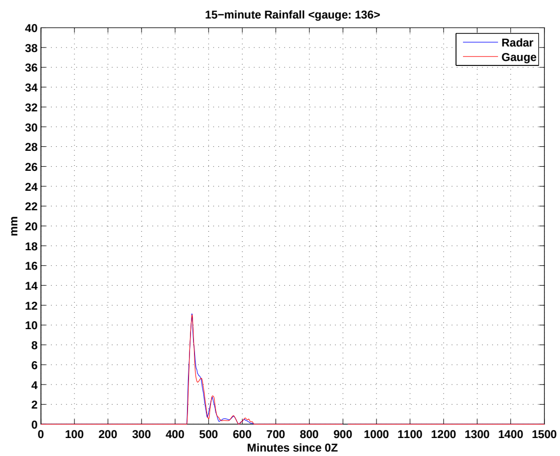

(c) 15-min rainfall point-wise trace

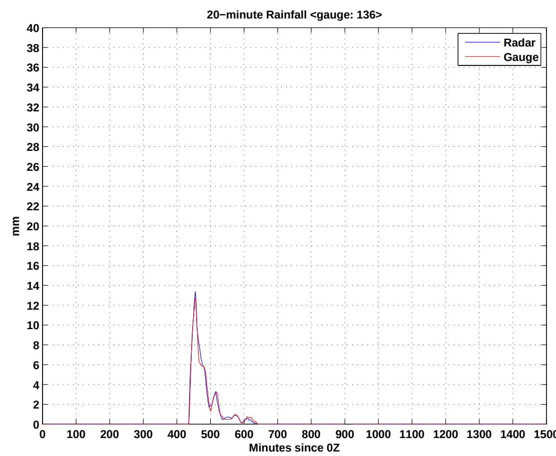

(d) 20-min rainfall point-wise trace

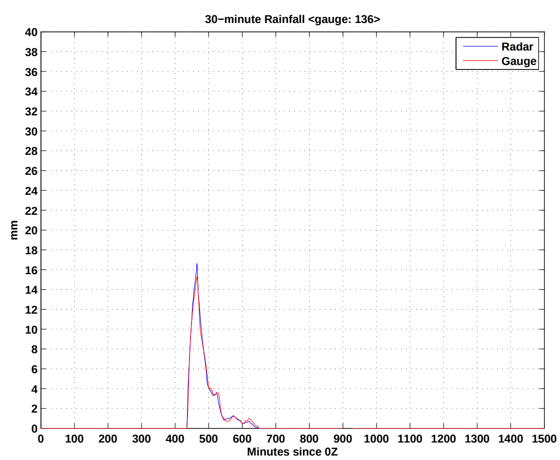

(e) 30-min rainfall point-wise trace

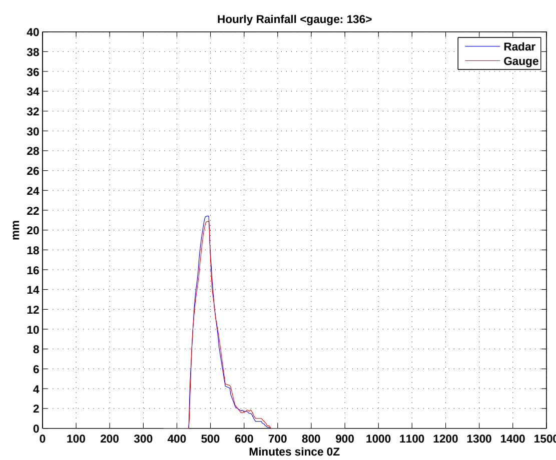

(f) 60-min rainfall point-wise trace

Figure 4.7: Point-wise line traces against gauges of June 14, 2007, storm event: at the location of gauge 136 (Latitude: 34.927800, Longitude: -97.965600).

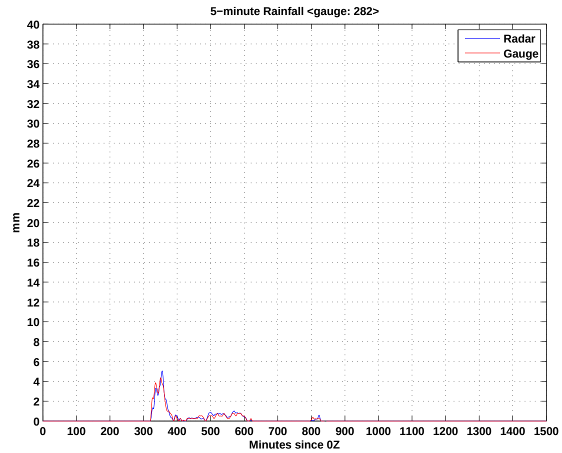

(a) 5-min rainfall point-wise trace

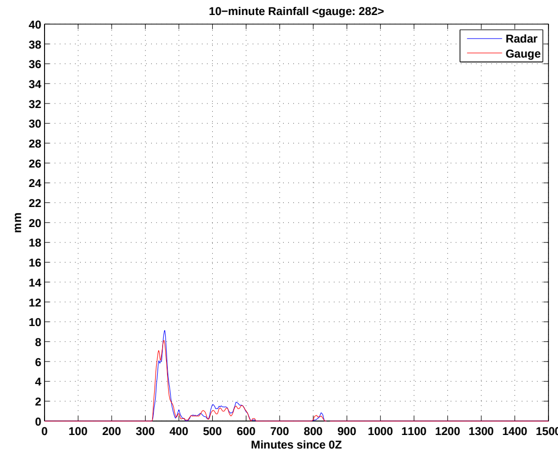

(b) 10-min rainfall point-wise trace

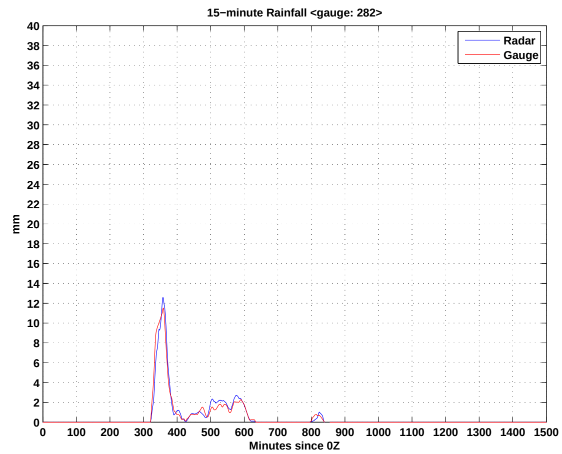

(c) 15-min rainfall point-wise trace

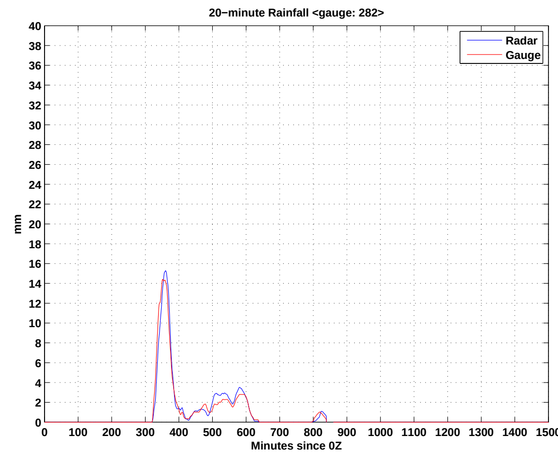

(d) 20-min rainfall point-wise trace

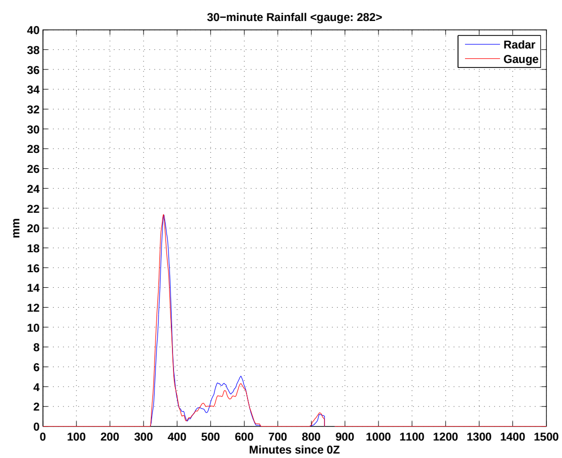

(e) 30-min rainfall point-wise trace

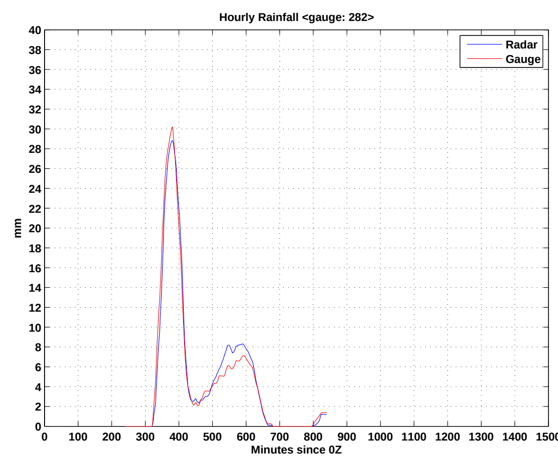

(f) 60-min rainfall point-wise trace

Figure 4.8: Point-wise line traces against gauges of June 20, 2007, storm event: at the location of gauge 282 (Latitude: 34.845039, Longitude: -98.073473).

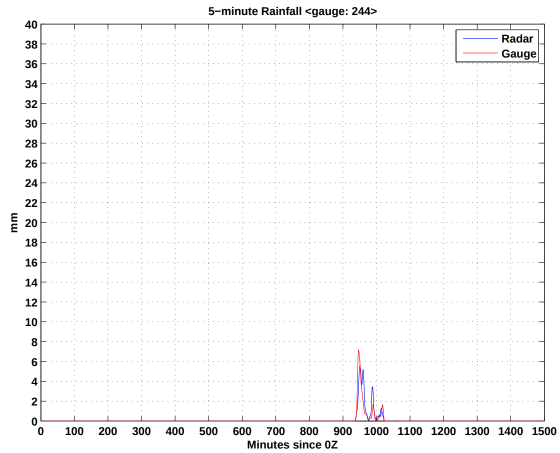

(a) 5-min rainfall point-wise trace

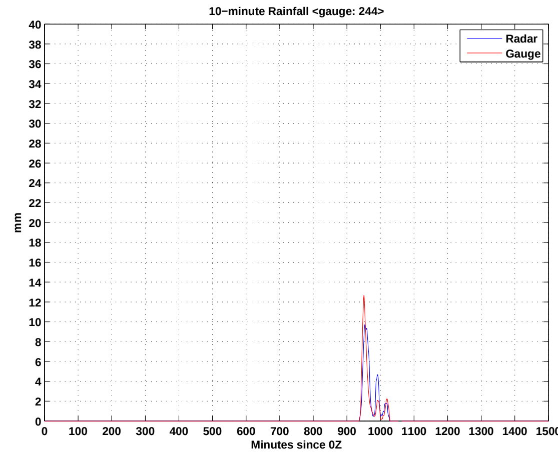

(b) 10-min rainfall point-wise trace

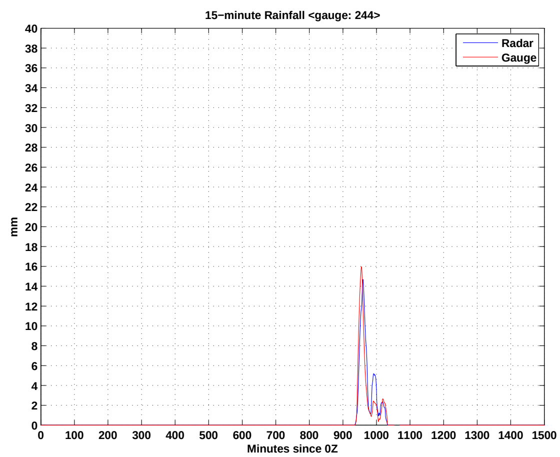

(c) 15-min rainfall point-wise trace

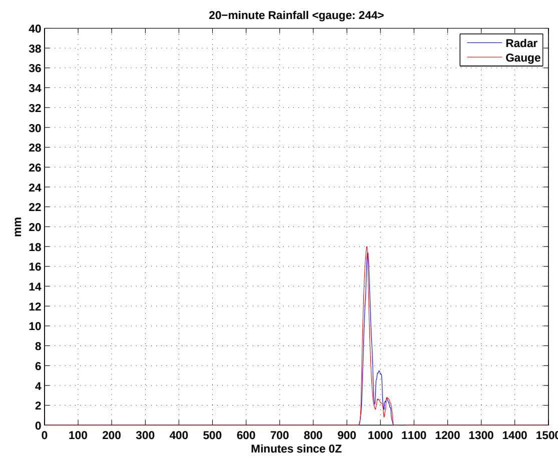

(d) 20-min rainfall point-wise trace

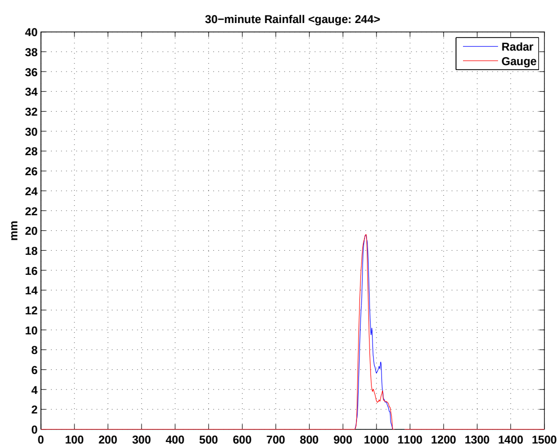

(e) 30-min rainfall point-wise trace

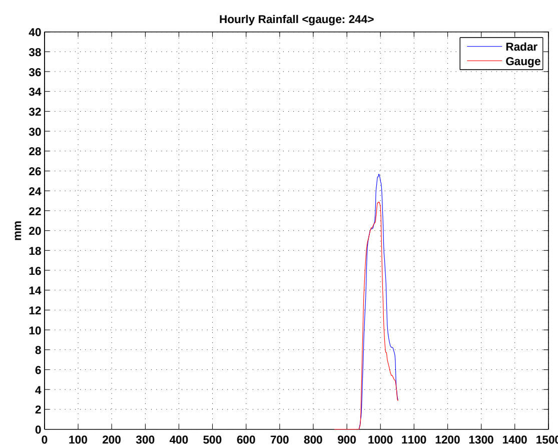

(f) 60-min rainfall point-wise trace

Figure 4.9: Point-wise line traces against gauges of May 05, 2009, storm event at the location of gauge 244 (Latitude: 34.860714, Longitude: -97.911140).

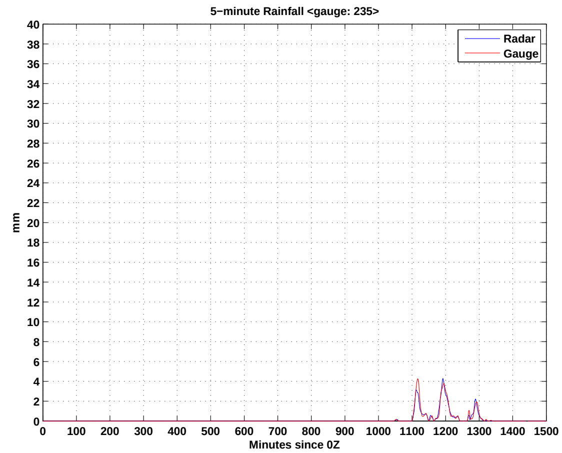

(a) 5-min rainfall point-wise trace

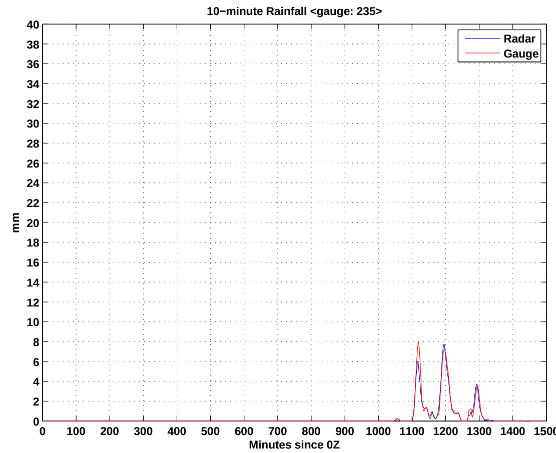

(b) 10-min rainfall point-wise trace

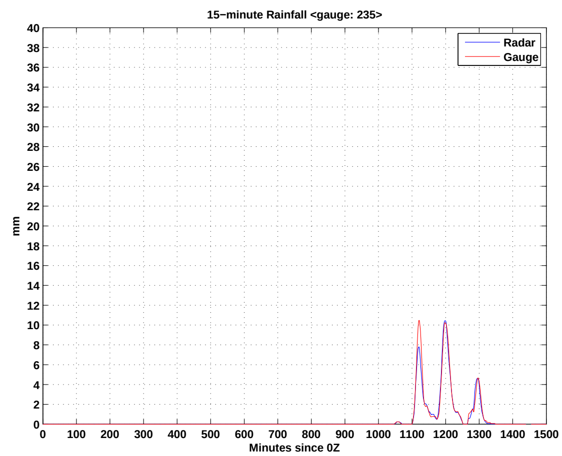

(c) 15-min rainfall point-wise trace

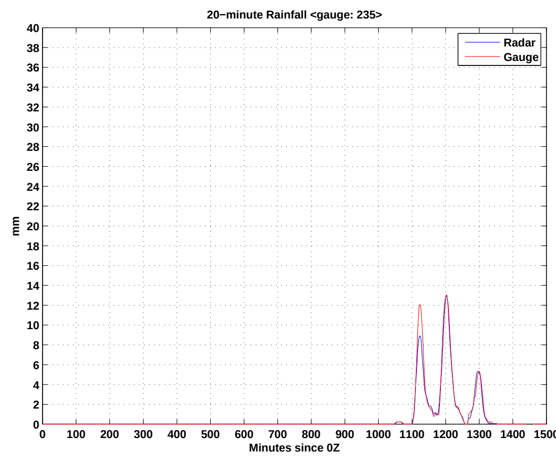

(d) 20-min rainfall point-wise trace

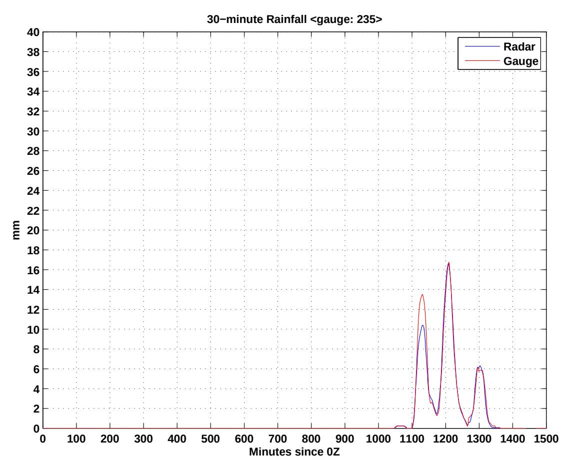

(e) 30-min rainfall point-wise trace

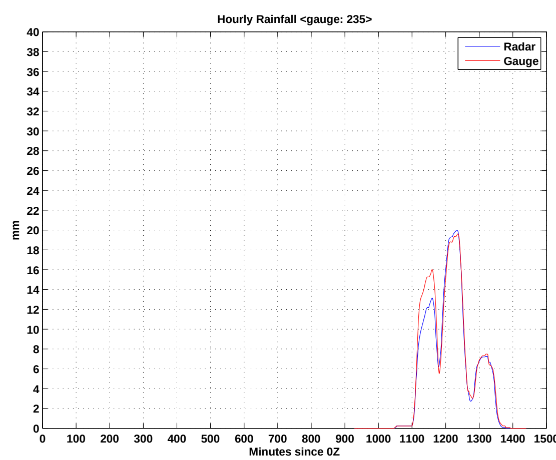

(f) 60-min rainfall point-wise trace

Figure 4.10: Point-wise line traces against gauges of June 14, 2010, storm event: at the location of gauge 235 (Latitude: 34.933460, Longitude: -98.018777).

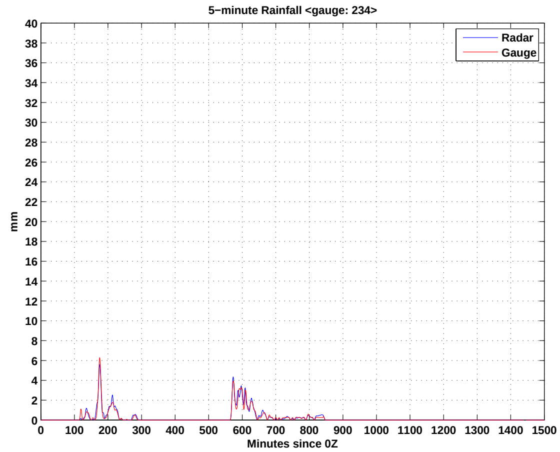

(a) 5-min rainfall point-wise trace

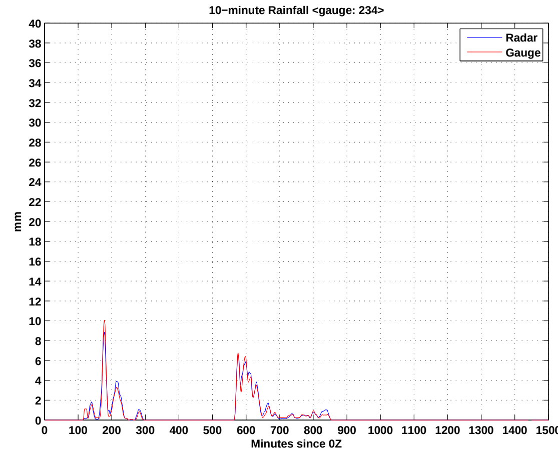

(b) 10-min rainfall point-wise trace

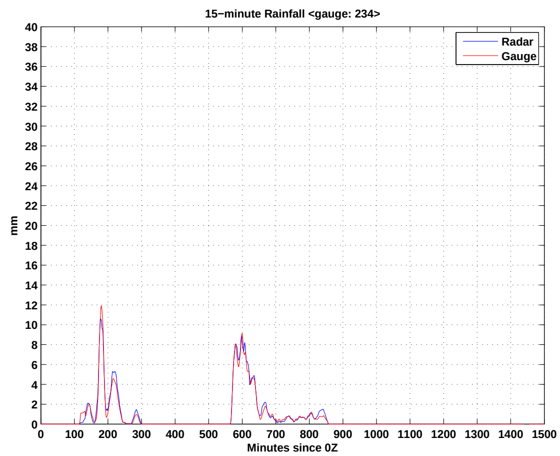

(c) 15-min rainfall point-wise trace

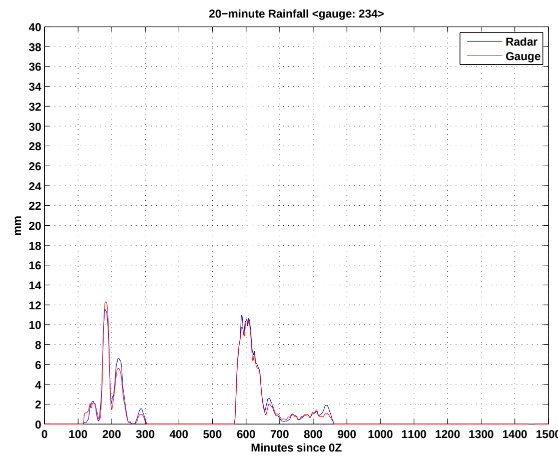

(d) 20-min rainfall point-wise trace

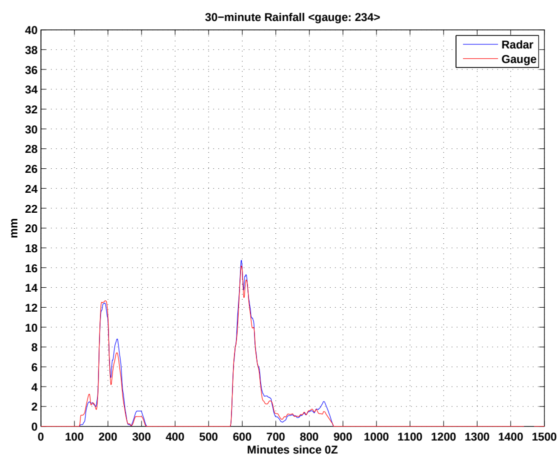

(e) 30-min rainfall point-wise trace

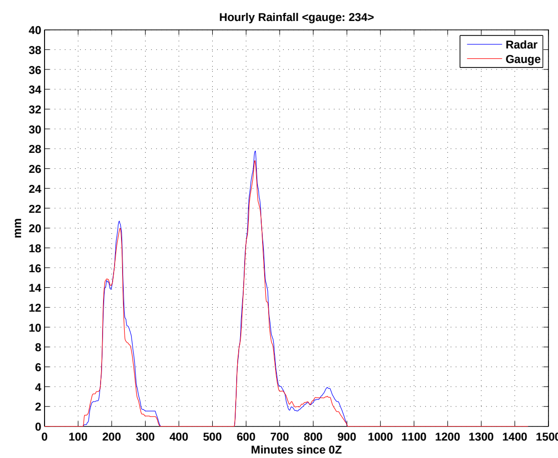

(f) 60-min rainfall point-wise trace

Figure 4.11: Point-wise line traces against gauges of May 20, 2011, storm event: at the location of gauge 234 (Latitude: 34.927445, Longitude: -98.075452).

4.2.2 Five-year Evaluation Results

For each storm event, the rainfall rate is estimated from networked radars and compared with the ground gauges. Figure 4.12 shows the rainfall rate distribution and corresponding statistical properties ("binned" mean) for the precipitation event of May 20, 2011. In addition, the 5-, 10-, 15, 20-, 30- and 60-minute rainfalls were also estimated and the color-coded density and "binned" mean plots were generated for each storm event. For the rainfall case on May 20, 2011, the "N"-minute rainfall distributions can be found in figure 4.13; the binned mean plots are shown in figure 4.14.

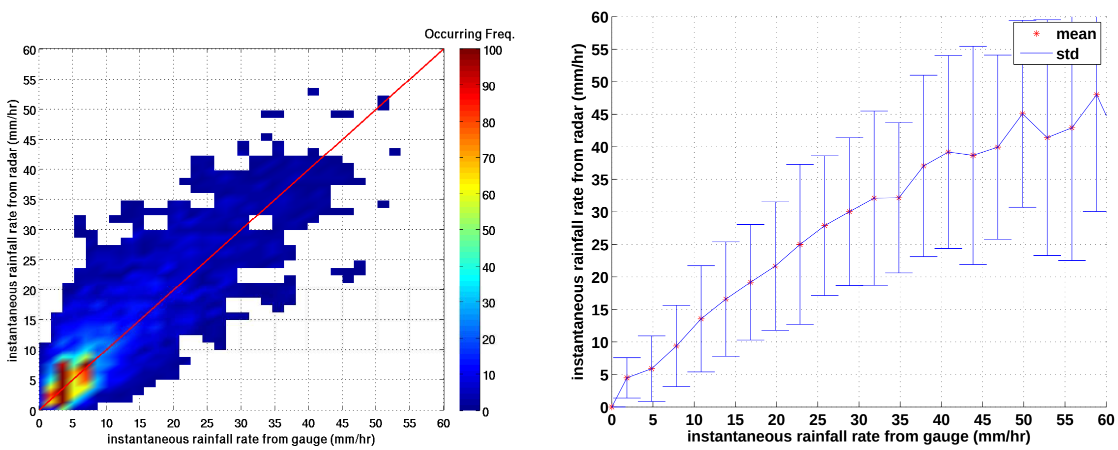

(a) rainfall rate distribution density comparison

(b) statistical properties comparison of rainfall rate

Figure 4.12: Event-wise rainfall rate distribution and statistical properties for May 20, 2011, storm case: radar vs. gauge.

Figure 4.15 shows the biases and standard error of the IP1 instantaneous rainfall rate estimates for all of the individual events. Similarly, Figure 4.16 and Figure 4.17 represent the event-wise biases and standard error of the "N"-minute rainfall estimates. From the biases scatter plots, it is easy to see that the instantaneous rainfall rate mostly has a bias within 3 mm/hr and the "N"-minute rainfall measurements mostly have biases within 1 mm. We can also see that the bias values do not have an overall trend with respect to the rainfall intensity of both instantaneous rain rate and period rainfall estimates (from gauges). There seems to be a general linearity between the standard error and the mean ground truth for both rainfall-rate and period rainfall estimates. As the mean instantaneous rain rate or the period rainfall intensities increases, the standard errors exhibit an increasing trend.

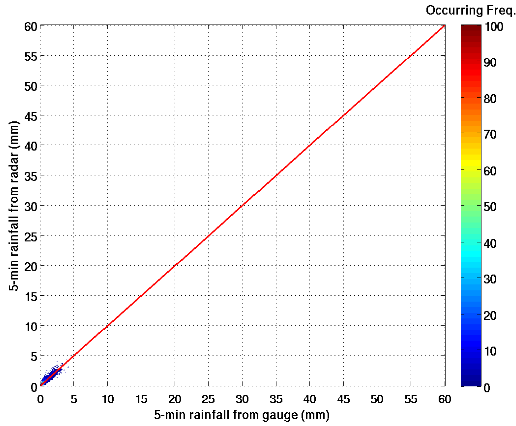

(a) 5-min rainfall distribution density comparison

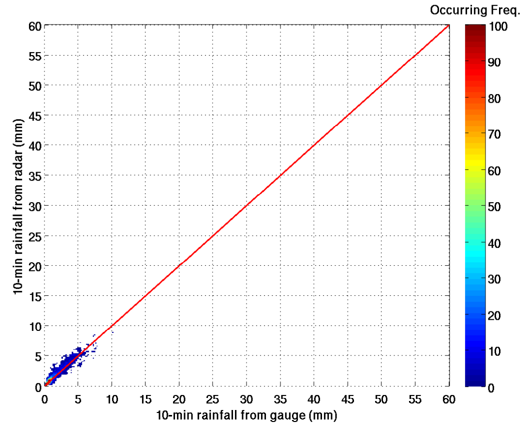

(b) 10-min rainfall distribution density comparison

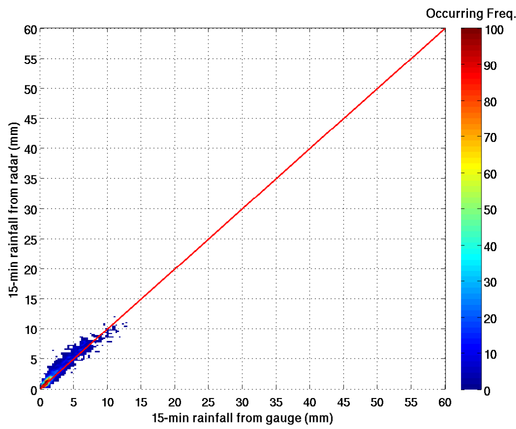

(c) 15-min rainfall distribution density comparison

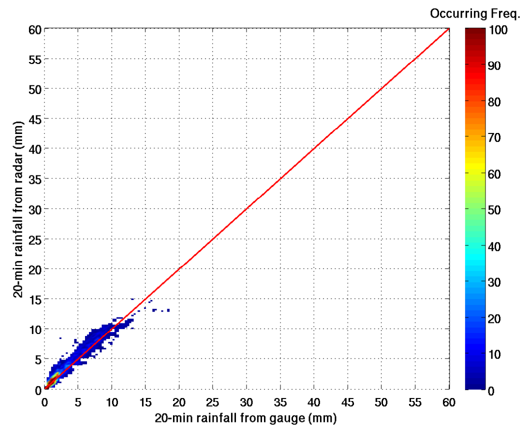

(d) 20-min rainfall distribution density comparison

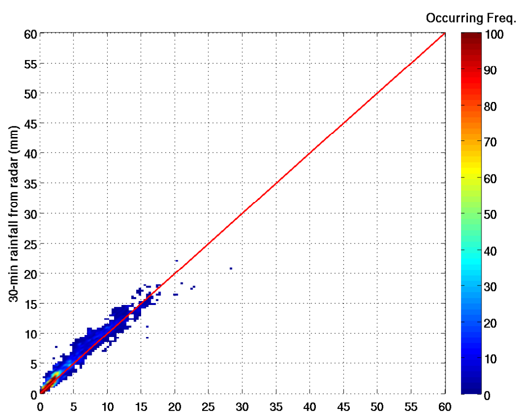

(e) 30-min rainfall distribution density comparison

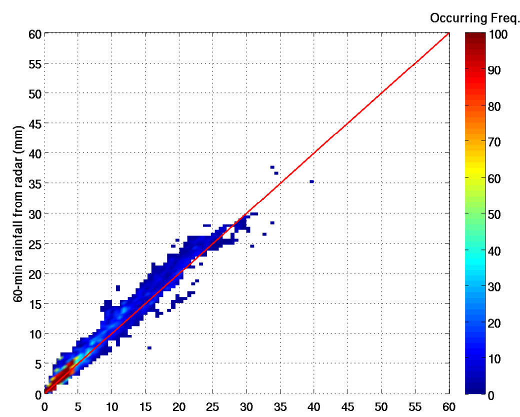

(f) 60-min rainfall distribution density comparison

Figure 4.13: Event-wise rainfall distribution density comparison for May 20, 2011, storm case: radar vs. gauge.

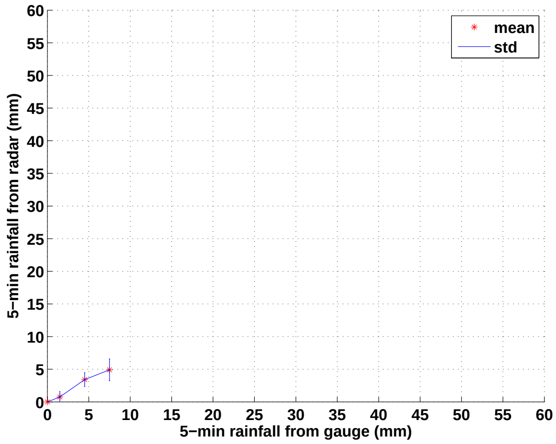

(a) statistical properties comparison of 5-min rainfall

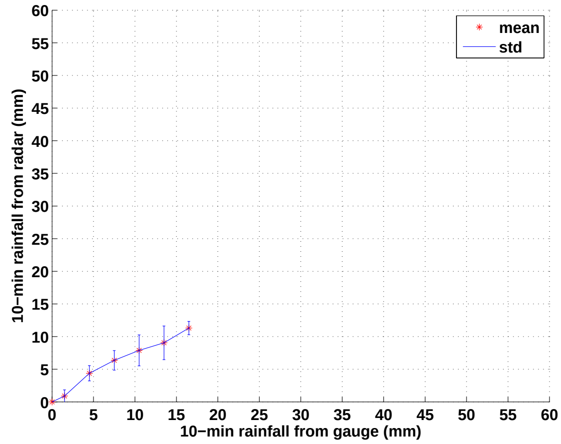

(b) statistical properties comparison of 10-min rainfall

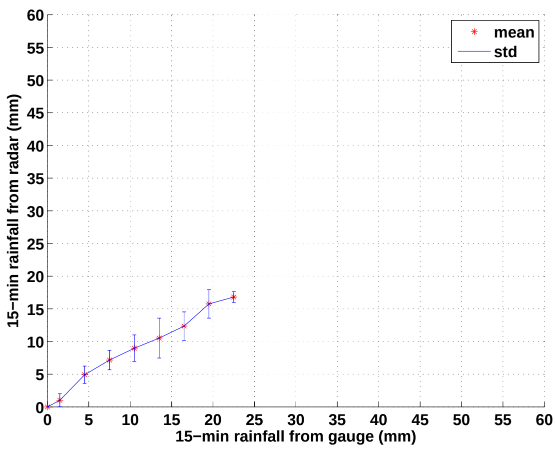

(c) statistical properties comparison of 15-min rainfall

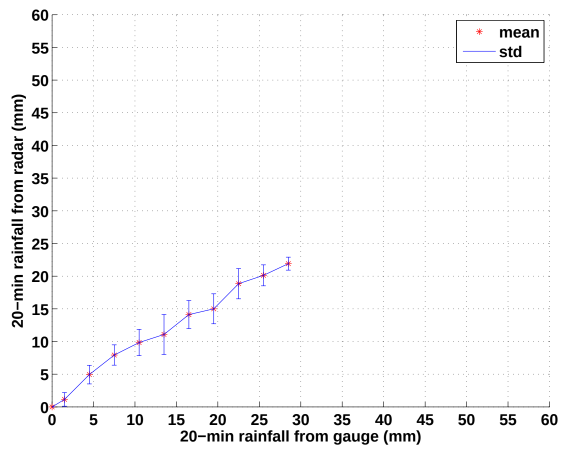

(d) statistical properties comparison of 20-min rainfall

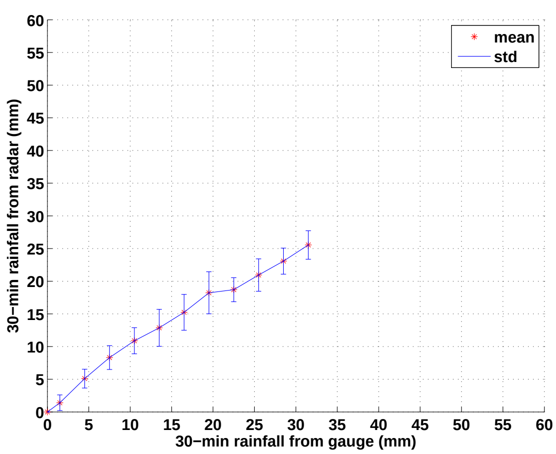

(e) statistical properties comparison of 30-min rainfall

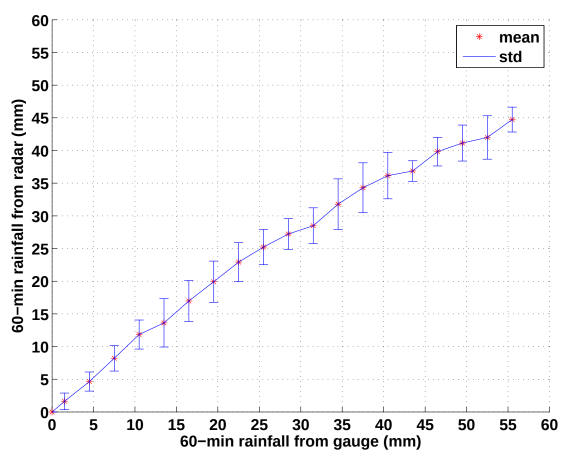

(f) statistical properties comparison of 60-min rainfall

Figure 4.14: Statistical properties of event-wise rainfall estimates for May 20, 2011, storm case.

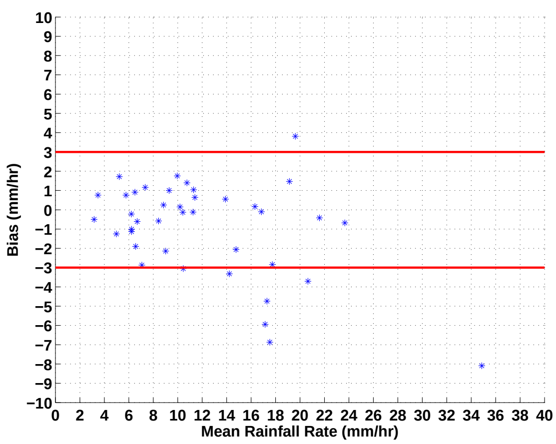

(a) rainfall rate biases

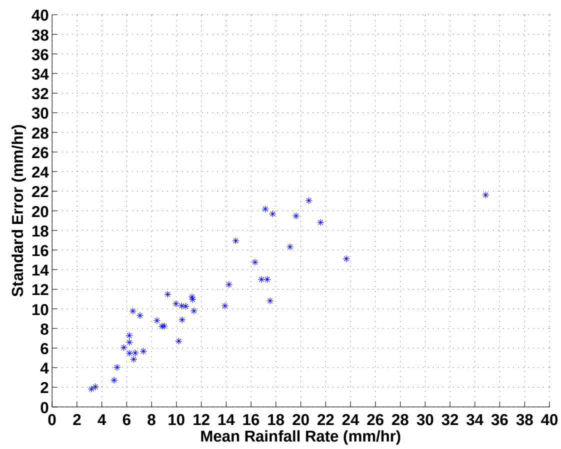

(b) standard error of rainfall rate estimates

Figure 4.15: Eventwise biases and standard error of the IP1 rainfall rate estimates.

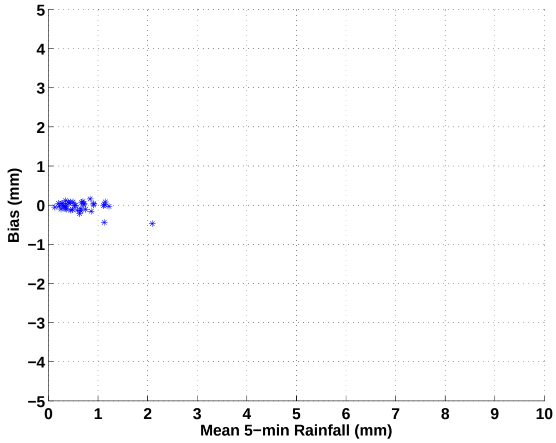

(a) 5-min rainfall biases

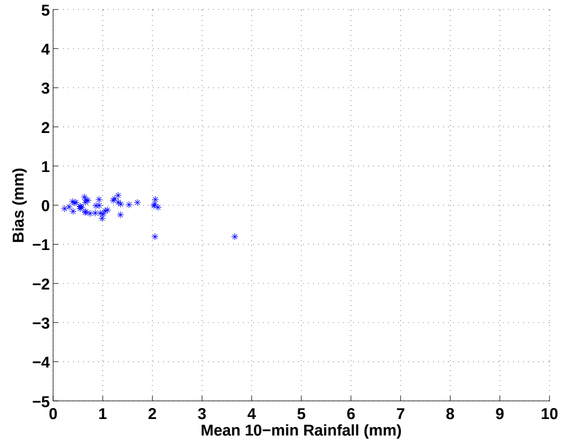

(b) 10-min rainfall biases

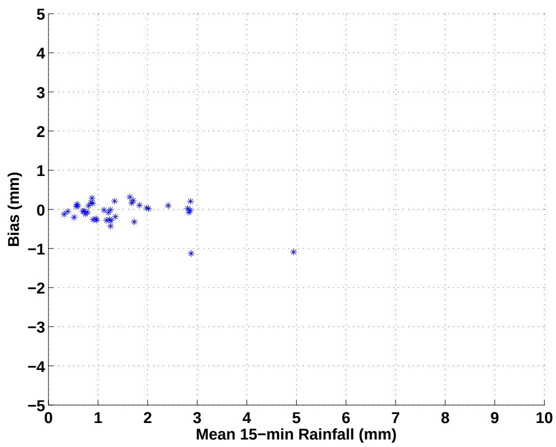

(c) 15-min rainfall biases

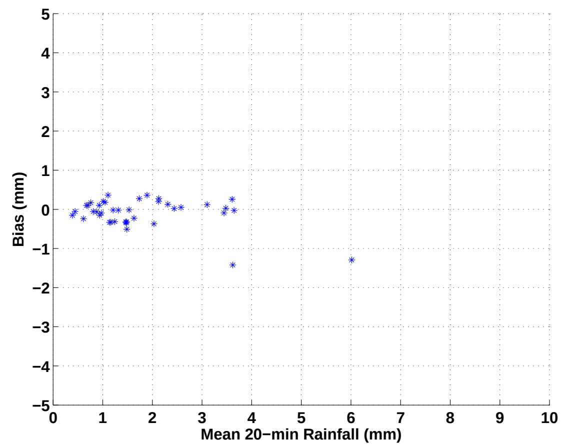

(d) 20-min rainfall biases

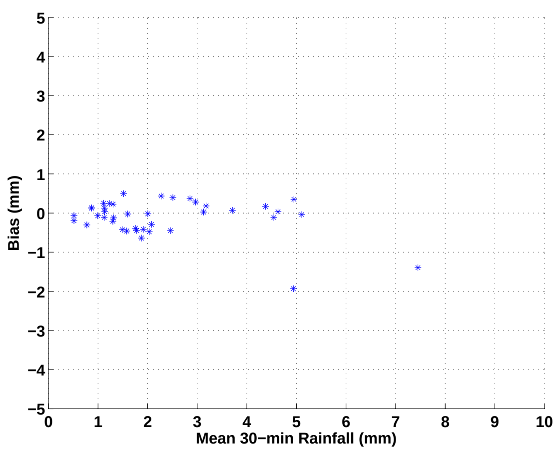

(e) 30-min rainfall biases

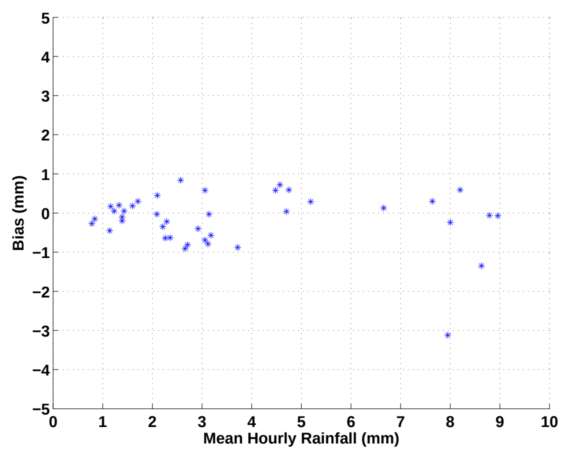

(f) 60-min rainfall biases

Figure 4.16: Eventwise biases of the IP1 rainfall estimates.

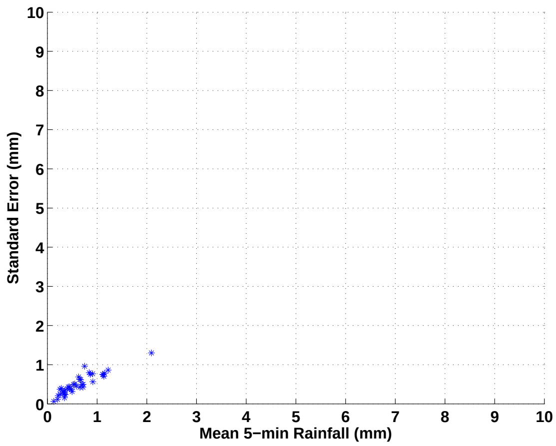

(a) standard error of 5-min rainfall

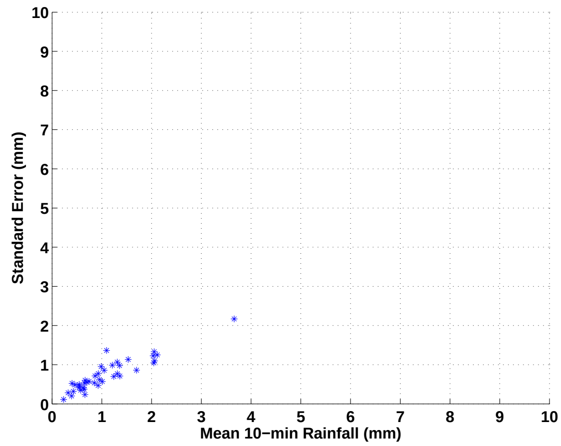

(b) standard error of 10-min rainfall

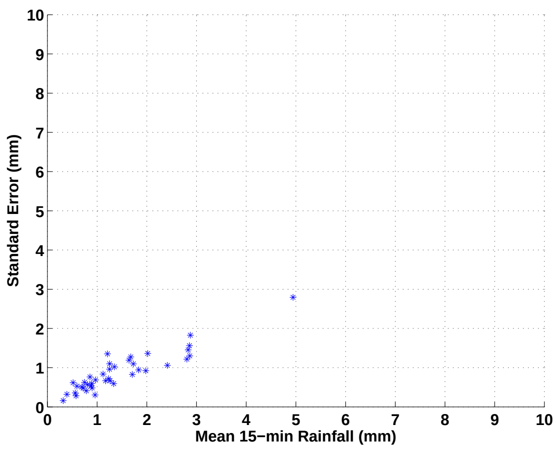

(c) standard error of 15-min rainfall

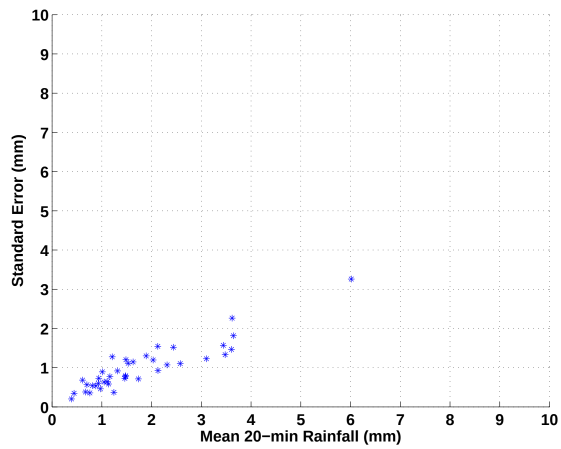

(d) standard error of 20-min rainfall

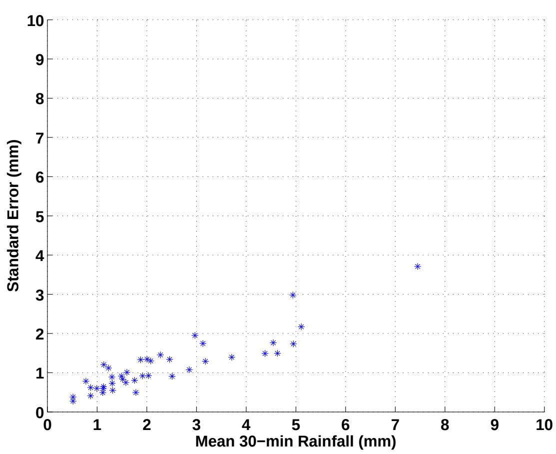

(e) standard error of 30-min rainfall

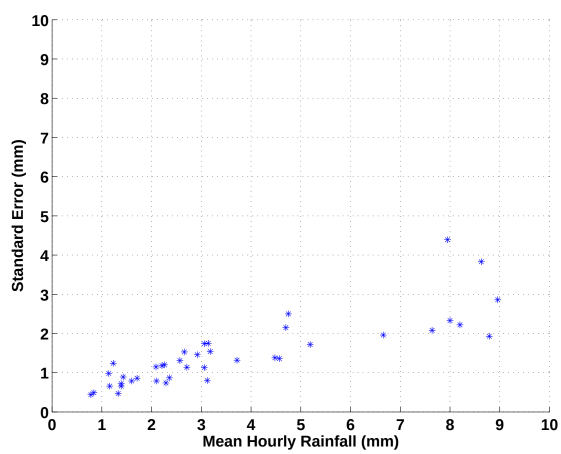

(f) standard error of 60-min rainfall

Figure 4.17: Standard error of the IP1 rainfall estimates.

The overall scores for 40 rainfall cases are computed based on the same performance metrics, taking into account the entire population. Obviously, this will give a higher weight for the longer-lasting events. As shown in table 4.2, the composite IP1 instantaneous rainfall rate has a fairly small bias of about -2.64% and an NSE about 49 % over all of the 40 precipitation events analyzed, and the estimates of 5- ,10-, 15-, 20-, 30- and hourly rainfall have normalized biases of about -2.53%, -2.49%, -2.45%, -2.40%, -2.29% and -2.21%, respectively, whereas low NSEs are about 40.86%, 35.81%, 32.93%, 31.17%, 28.96% and 25.14% respectively. These performance evaluation results demonstrate a great improvement compared to the current state-of-the-art.

Table 4.2: Overall performance of K_{dp}-based CASA QPE algorithms.

Rainfall Estimates	**Total Events Analyzed**	**Normalized Bias (%)**	**NSE (%)**
Instantaneous rain rate	40	-2.64	49.00
5-min rainfall	40	-2.53	40.86
10-min rainfall	40	-2.49	35.81
15-min rainfall	40	-2.45	32.93
20-min rainfall	40	-2.40	31.17
30-min rainfall	40	-2.29	28.96
60-min (hourly) rainfall	40	-2.21	25.14

4.3 Summary

A five-year evaluation study has been conducted in this chapter. From the validation results from 40 rainfall events, we concluded that the CASA QPE system is an excellent tool for precipitation measurements. In addition, various rainfall measurement products were also given in this chapter. These rainfall products are critical candidates for hydrological input for future hydrologic and hydraulic analysis.

CHAPTER 5

SUMMARY AND CONCLUSIONS

5.1 Summary

In recent years, X-band (8-12 GHz) radar has gained increasing interest for use in weather sensing because of its shorter wavelength and lower cost. The National Science Foundation Engineering Research Center (NSF-ERC) for Collaborative and Adaptive Sensing of the Atmosphere (CASA) has developed a dual-polarization X-band radar network for detecting the region of the lower atmosphere that is currently below conventional radar range. The need for a study of the quantitative precipitation estimation (QPE) by such a dual-polarization X-band radar network is essential. In this thesis, the dual-polarization rainfall estimation system developed by CASA was studied.

This research begins with a description of the CASA radar network and its operational methodology. Today's weather radar network such as the National Weather Service's (NWS) Weather Surveillance Radar-1988 Doppler (WSR-88D) network, also known as Next-Generation Radar (NEXRAD) network, and the Federal Aviation Administration's (FAA) Terminal Doppler Weather Radar (TDWR) network use either S-band (2-4 GHz) or C-band (4-8 GHz) radars to detect precipitations, atmospheric movement, and hazardous wind shear conditions. However, these high-power, long-range radars have limited ability to observe the lower part of the atmosphere because of the earth curvature effect. As a result, meteorological conditions in the lower atmosphere will be under-sampled. Thus, it is challenging to make accurate estimations and predictions of hazardous weather events in this region. By deploying the lower-cost and smaller X-band radars, CASA is able to see the lower troposphere. Installed just about 30 km apart, these small radars can communicate with each other and adjust their scanning modes in response to quickly changing weather and different users' needs. Through the distributed collaborative adaptive sensing (DCAS) operational methodology developed by CASA, the radars work collaboratively within a dynamic information technology infrastructure, conducting high-resolution sensing and accurate predictions. Up-to-the-second radar information can then be used to make critical decisions about the weather and to issue important warnings. The accomplishments, breakthroughs, and lessons learned from the past five-years' operation were also presented in this thesis. The first urban demonstration network of CASA in the Dallas-Fort Worth area was briefly described in Chapter 2.

This thesis focuses on the development and evaluation of the CASA QPE system. Before getting into the details of CASA QPE system, the rainfall drop size distribution (DSD) models and commonly used rainfall algorithms were reviewed in Chapter 3. The algorithms include traditional $Z - R$ relations, K_{dp}-based algorithm, and a couple of hybrid algorithms. The dual-polarization radar QPE system developed by CASA was then introduced in depth. The high spatio-temporal resolution CASA QPE is based on the measurement of a specific differential phase (K_{dp}). Unlike the rainfall estimation based on the power products such as Z and Z_{dr}, K_{dp}-based QPE is less sensitive to the DSD. Another advantage of relying on K_{dp} to estimate rainfall is that it is relatively less prone to calibration errors. Being the range derivative of the differential phase shift, K_{dp} is less susceptible to path attenuation. The $R - K_{dp}$ estimator is also immune to partial beam blockage and hail contamination. The use of network radars gives rise to a more accurate rainfall estimation: since more data are collected from different viewing aspects, a more conclusive set of K_{dp} can be obtained. To validate the CASA QPE products, a network of 20 rainfall gauges were used for cross-comparison. The rainfall measurements from the 20 rainfall gauges are archived as accumulations at five-minute intervals over every 24-hour period, with a resolution of 0.254 mm. The gauge data format and rainfall evaluation metrics were presented. The various sensing aspects for CASA QPE and the estimation of K_{dp} were also described in Chapter 3.

Sample rainfall products such as the hourly rainfall maps and point-wise line traces of rainfall estimates are given in Chapter 4. In addition, a five-year validation study of the CASA QPE system was conducted. Rainfall measurements from 40 precipitation events were used for cross comparisons. Over all of the 40 precipitation events, the composite IP1 instantaneous rainfall rate has a fairly small bias of about -2.64 % and an normalized standard error (NSE) of about 49% and the estimates of 5- ,10-, 15-, 20-, 30- and 60-minute rainfall have normalized biases of about -2.53%, -2.49%, -2.45%, -2.40%, -2.29% and -2.21%, respectively, whereas they have low NSEs of about 40.86%, 35.81%, 32.93%, 31.17%, 28.96% and 25.14%, respectively. These evaluation scores show that the CASA QPE system is a great improvement compared to the current state-of-the-art system.

Overall, this thesis has presented a comprehensive evaluation and description of the CASA QPE system. The sample rainfall products and evaluation studies provided here show that the system has satisfactory operation and is capable of providing accurate, high-resolution rainfall measurements that can be used for flash flood warning and mitigation.

5.2 Future Work

Although an extensive description and evaluation of the CASA QPE system has been given, this work can be extended in several ways. Some of these extensions are sensitivity analysis, hydrological application of CASA QPE products, and the development of multi-sensor precipitation estimation methodology.

5.2.1 Sensitivity Analysis

When the rainfall intensity is very small, say less than 0.3 mm/hr, the estimation of specific differential propagation phase (K_{dp}) becomes more difficult. It is entirely possible that the K_{dp} will be drowned in the noise, which will make the rainfall measurements unreliable and inaccurate. One possible solution to this problem is to study the reflectivity estimates and properties in those rain cells. However, the combination of the reflectivity field will make the QPE system more complicated, which will delay the response of the hydrological models and emergency management. The sensitivity of CASA QPE system needs further analysis to reach its full capacity.

5.2.2 Hydrological Applications

Radar quantitative precipitation estimation has a great potential to drive the hydrologic models for runoff estimation and flood monitoring, prediction, and mitigation ([53], [54]). Accurate rainfall measurements are a prerequisite for stream flow simulations. The impacts of radar QPE on hydrological models have gained increasing attention in recent years, but most of the studies are concentrated on S-, or C-band radar observations. The high-resolution rainfall products from CASA X-band radar QPE system and rainfall nowcasting products from CASA can serve as a reliable data input for distributed hydrological models so as to assess the impacts of dual- polarization X-band radars on flash flood monitoring and forecasting. Figure 5.1 is a closed-loop architecture showing the important role of CASA QPE and short-term QPF for urban flash flood applications [55].

The Hydrology Laboratory-Research Distributed Hydrologic Model (HL-RDHM) developed by the U.S. National Weather Service (NWS) Office of Hydrologic Development (OHD) is a great tool for generating

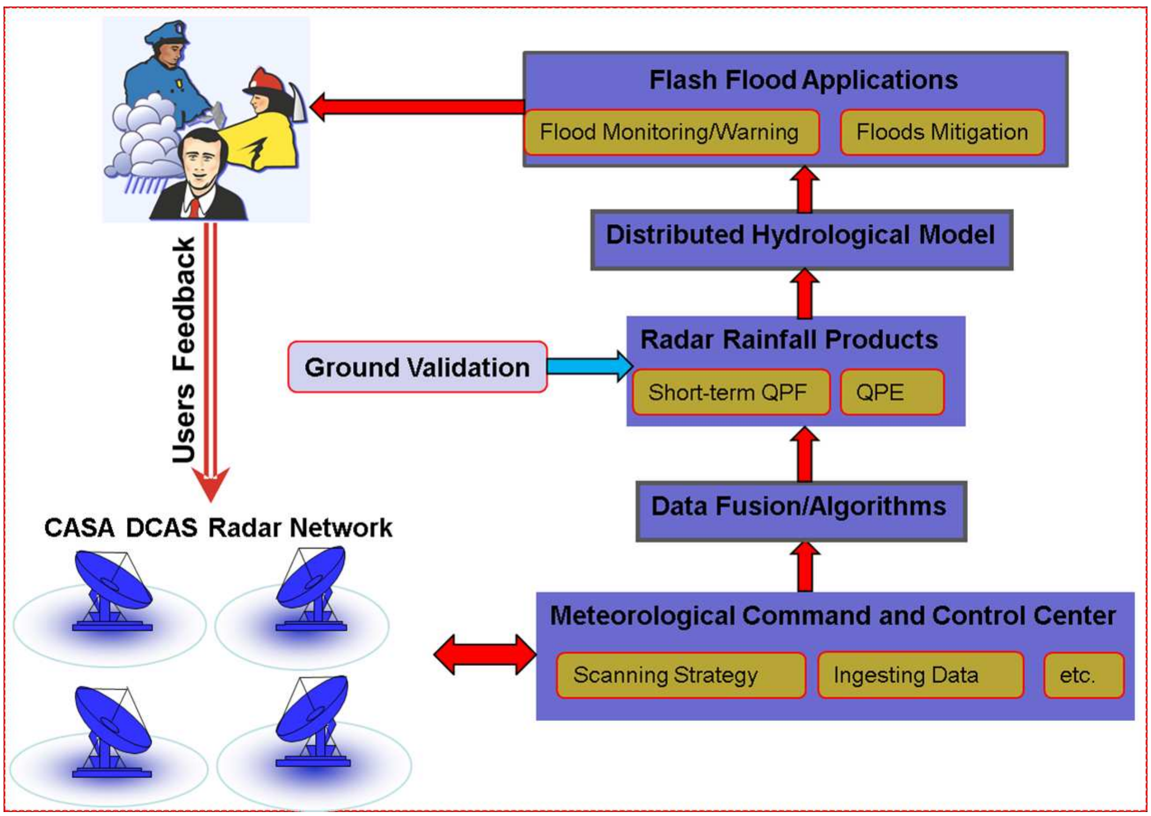

Figure 5.1: Closed loop of urban flash flood monitoring system based on the X-band dual-polarization radar network.

runoff and other hydrological information such as soil moisture, etc ([56]). Currently, this model is being tested using hourly rainfall estimates produced by the CASA X-band dual-polarization radar network for the purpose of flash flood applications. In addition, the Hydrologic Modeling System (HMS) designed in the U.S. Army Corps of Engineers (USACE) Hydrologic Engineering Center (HEC) can also simulate the precipitation-runoff processed in dendritic watershed systems (see $http://www.hec.usace.army.mil/software/hec-hms/$). The HEC-HMS is applicable in a wide range of geographic regions for studies of water availability, urban drainage, stream flow forecasting, reservoir spillway design, and systems operation. CASA will also adopt the HEC-HMS in the Dallas-Fort Worth metropolitan area. The impacts of CASA QPE on HL-RDHM and HEC-HMS will be focused on in future research. Understanding the uncertainties of radar QPE and hydrological modelling is another essential step in the future research.

5.2.3 Multisensor Precipitation Estimation

Beyond the accurate high-resolution CASA QPE products, we still have many problems related to estimating precipitation in many remote parts of the world and particularly in developing countries. QPE is extremely challenging in areas of complex terrain such as the western United States due to the sparse coverage of ground-based meteorological radars and the effects of beam blockage (e.g., [57]). The combination of different instruments for rainfall measurements has been focused world wide to provide rainfall maps of good orographic coverage. The Multisensor Precipitation Estimator (MPE) [58] [59] and National Mosaic and Multi-sensor QPE (NMQ) [60], developed by NWS and NSSL, respectively, are good examples of such combinations. Both can produce gridded QPE products that include radar-only, gauge-only, and gauge-radar-mosaiced, and so forth. How to combine the CASA QPE system with satellite and regional rain gauge measurements to get an optimal rainfall estimate is another topic to be followed in future research.

REFERENCES

[1] D. McLaughlin and Coauthors, 2009: Short-Wavelength Technology and the Potential For Distributed Networks of Small Radar Systems. *Bull. Amer. Meteor. Soc.*, 90, 1797-1817.

[2] Merrill. I. Skolnik, *Introduction to Radar Systems*, McGraw Hill Book Company, Inc., New York, 1962.

[3] E. V. Appleton and M. A. F. Barnett, On Some direct Evidence for Downward Atmospheric Reflection Of Electric Rays. *Proceedings of the Royal Society*, A 109, 621-641, 1925.

[4] G. Breit and M. A. Tuve, A Test of the Existence of the Conducting Layer.*Phys. Rev.*, 28, 554-575,1926

[5] V. N. Bringi and V. Chandrasekar Bringi, 2001: *Polarimetric Doppler Weather Radar: Principles and Applications*. Cambridge University Press, 648 pp.

[6] J. Brotzge, V. Chandresakar, K. Droegemeier, J. Kurose, D. McLaughlin, B. Philips, M. Preston, S. Sekelsky, 2004: Distributed Collaborative Adaptive Sensing for Hazardous Weather Detection, Tracking, and Predicting, *Proceedings of the 4th International Conference on Computational Science (ICCS 2004)*, Krakow, Poland, June 6-9, 2004.

[7] V. Chandrasekar, S. Lim, 2008: Retrieval of Reflectivity in a Networked Radar Environment. *J. Atmos. Oceanic Technol.*, 25, 1755-1767.

[8] Sean X. Zhang, 2011: CASA REAL-TIME MULTI-DOPPLER RETRIEVAL SYSTEM, *Thesis for Master of Science*, Colorado State University.

[9] Evan Ruzanski, V. Chandrasekar and Yanting Wang, 2011: The CASA Nowcasting System.*J. Atmos. Oceanic Technol.*, 28, 640-655.

[10] D. J. Rude, E. J. Bass and B. Philips, 2009: Impact of Increased Spatio-Temporal Radar Data Resolution on Forecaster Wind Assessments, *2009 IEEE Conference on Systems, Man, and Cybernetics* ., San Antonio, TX.

[11] V. Chandrasekar, David McLaughlin, Brenda Philips, Mike Zink, Jerry Brotzge, Yanting Wang, Sanghun Lim, Francesc Junyent, Nitin Bharadwaj, Eric Lyons, and David Westbrook, 2010: The CASA IP1 test-bed after 5 years operation: Accomplishments, breakthroughs, challenges and lessons learned, *Proc. of the 6th European Conf. on Radar in Meteorology and Hydrology*, Sibiu, Romania

[12] Evan Ruzanski and V. Chandrasekar, 2012: Nowcasting rainfall fields derived from specific differential phase. *J. Appl. Meteor. Climatol.*, doi:10.1175/JAMC-D-11-081.1, in press.

[13] Raymond Wexler, 1947: Radar Detection of A Frontal Storm. *J. Meteor.*, 4, 38-44.

[14] J. S. Marshall, R. C. Langille and W. Mc K. Palmer, 1947: Measurement of Rainfall by Radar. *J. Meteor.*, 4, 186-192.

[15] Robert Cifelli and V. Chandrasekar, 2010: Dual polarization radar rainfall estimation. *Rainfall: State of the Science*, F.Y. Testik and M. Gebremichael, Eds., *Amer. Geophys. Union*, 105-125, 10.1029/2010GM001026.

[16] J. S. Marshall and W. McK. Palmer, 1948: The Distribution of Raindrops with Size. *J. Meteor.*, 5, 165-166.

[17] A. Waldvogel, 1974: The N_0 jump of raindrop spectra. *J. Atmos. Sci.*, 31, 1067-1078.

[18] C. W. Ulbrich, 1983: Natural variations in the analytical form of the raindrop size distribution. *J. Climate Appl. Meteor.*,22, 1764-1775.

[19] A. Tokay and D. A. Short, 1996: Evidence from tropical raindrop spectra of the origin of rain from stratiform versus convective clouds. *J. Appl. Meteor.*, 35, 355-371.

[20] E. Gorgucci, V. Chandrasekar, V. N. Bringi and Gianfranco Scarchilli, 2002: Estimation of Raindrop Size Distribution Parameters from Polarimetric Radar Measurements.*J. Atmos. Sci.*, 59, 2373-2384.

[21] C. R. Williams and K. S. Gage, 2009: Raindrop size distribution variability estimated using ensemble statistics. *Ann. Geophys.*, 27, 555-567.

[22] Anthony J. Illingworth and T. Mark Blackman, 2002: The Need to Represent Raindrop Size Spectra as Normalized Gamma Distributions for the Interpretation of Polarization Radar Observations. *J. Appl. Meteor.*, 41, 286-297.

[23] Edward A. Brandes, Guifu Zhang and J. Vivekanandan, 2003: An Evaluation of a Drop Distribution-Based Polarimetric Radar Rainfall Estimator. *J. Appl. Meteor.*, 42, 652-660.

[24] Guifu Zhang, J. Vivekanandan, Edward A. Brandes, Robert Meneghini and Toshiaki Kozu, 2003: The ShapeSlope Relation in Observed Gamma Raindrop Size Distributions: Statistical Error or Useful Information?. *J. Atmos. Oceanic Technol.*, 20, 1106-1119.

[25] G. Feingold and Z. Levin, 1986: The lognormal fit to raindrop spectra from frontal convective clouds in Israel. *J. Clim. Appl. Meteor.*, 25, 1346-1363.

[26] D. Atlas, R. C. Srivastava and R. S. Sekron, 1973: Doppler radar characteristics of precipitation at vertical incidence. *Rev. Geophys. Space Phys.*, 11, 1-35.

[27] D. Atlas, Carlton W. Ulbrich, 1977: Path- and Area-Integrated Rainfall Measurement by Microwave Attenuation in the 13 cm Band.*J. Appl. Meteor.*, 16, 1322-1331.

[28] Louis J. Battan, 1973: *Radar Observation of the Atmosphere*. University of Chicago Press, Chicago, 324 pp.

[29] Y. Wang and V. Chandrasekar, 2009: Algorithm for Estimation of the Specific Differential Phase. *J. Atmos. Oceanic Technol.*, 26, 2565-2578.

[30] J. Hubbert, V. Chandrasekar, V. N. Bringi, and P. F. Meischner, 1993: Processing and interpretation of coherent dual-polarized radar measurements. *J. Atmos. Oceanic Technol.*, 10, 155-164.

[31] J. Hubbert and V. N. Bringi, 1995: An iterative technique filtering technique for the analysis of copolar differential phase and dual-frequency polarimetric variables. *J. Atmos. Oceanic Technol.*, 12, 643-648.

[32] T. Otto and H. W. J. Russchenberg, 2011: Estimation of specific differential phase and differential backscatter phase from polarimetric weather radar measurements of rain. *IEEE Geosci. Remote Sens. Lett.*, 8, 988-992.

[33] M. Schneebeli and A. Berne, 2012: An extended Kalman filter framework for polarimetric X-band weather radar data processing. *J. Atmos. Oceanic Technol.*, 29, 711-730.

[34] Carlton W. Ulbrich and D. Atlas. 1998. Rainfall microphysics and radar properties: Analysis methods for drop size spectra. *J. Appl. Meteor.*, 37, 912-923.

[35] E. Gorgucci, G. Scarchilli and V. Chandrasekar, 1994: A robust estimator of rainfall rate using differential reflectivity. *J. Atmos. Oceanic Technol.*, 11, 586-592.

[36] Kenneth V. Beard and Catherine Chuang, 1987: A New Model for the Equilibrium Shape of Raindrops. *J. Atmos. Sci.*, 44, 1509-1524.

[37] E. Gorgucci and G. Scarchilli, 1997: Intercomparison of multiparameter radar algorithms for estimating of rainfall rate. *In Preprints of 28th Conf. on Radar Meteorology*, Boston, MA, American Meteorology Society.

[38] Robert Cifelli, V. Chandrasekar, S. Lim, P. C. Kennedy, Y. Wang and S. A. Rutledge, 2011: A New Dual-Polarization Radar Rainfall Algorithm: Application in Colorado Precipitation Events. *J. Atmos. Oceanic Technol.*, 28, 352-364.

[39] A. V. Ryzhkov, Scott E. Giangrande, Terry J. Schuur, 2005: Rainfall Estimation with a Polarimetric Prototype of WSR-88D. *J. Appl. Meteor.*, 44, 502-515.

[40] S. Lim, V. Chandrasekar and V. N. Bringi, 2005: Hydrometeor classification system using dual-polarization radar measurements: Model improvements and in situ verification. *IEEE Trans. Geosci. Remote Sens.*, 43, 792801.

[41] Elena Saltikoff, A. Huuskonen, H. Hohti, J. Koistinen and H. Jrvinen, 2010: Quality assurance in the FMI Doppler Weather Radar Network. *Boreal Env. Res.*, 15, 579594.

[42] M. Maki and Coauthors, 2008: X-band polarimetric radar network in the Tokyo Metropolitan area—X-NET. *Proc. of Fifth European Conf. on Radar Meteorology*, Helsinki, Finland.

[43] Alexander V. Ryzhkov, 2007: The Impact of Beam Broadening on the Quality of Radar Polarimetric Data. *J. Atmos. Oceanic Technol.,* 24, 729-744.

[44] J. Zhang and Y. Qi, 2010: A Real-Time Algorithm for the Correction of Brightband Effects in Radar-Derived QPE. *J. Hydrometeor.,* 11, 1157-1171.

[45] F. Junyent and V. Chandrasekar, 2009: Theory and characterization of weather radar networks. *J. Atmos. Ocean. Technol.*, 26, 474-491.

[46] M. Zink, E. Lyons, D. Westbrook, J. Kurose and D. Pepyne, 2010: Closed-loop Architecture for Distributed Collaborative Adaptive Sensing of the Atmosphere: Meteorological Command & Control. *International J. Sensor Networks*, 7, No. 1/2, 4-18.

[47] V. Chandrasekar, Y. Wang and H. Chen, 2012: The CASA quantitative precipitation estimation system: a five year validation study. *Nat. Hazards Earth Syst. Sci.*, 12, 2811-2820.

[48] A. D. Siggia and R. E. Passarelli, 2004: Gaussian model adaptive processing (GMAP) for improved ground clutter cancellation and moment calculation. *Proc. of 3rd European Conf. on Radar in Meteorol. and Hydrology*, Visby, Sweden.

[49] V. Chandrasekar, D. McLaughlin, J. Brotzge, M. Zink, B. Philips and Y. Wang, 2008: Distributed collaborative adaptive radar network: Preliminary results from the CASA IP1 testbed. *Proc. of 2008 IEEE Radar Conf.,* Rome, Italy.

[50] V. Chandrasekar, D. Willie, Y. Wang, S. Lim and D. McLaughlin, 2009: Attenuation margin requirements in a networked radar system for observation of precipitation. *IEEE Int. Geoscience and Remote Sensing Symp.(IGARSS 2009),* Cape Town, South Africa.

[51] D. S. Zrni and A. Ryzhkov, 1996: Advantages of Rain Measurements Using Specific Differential Phase. *J. Atmos. Oceanic Technol.*, 13, 454-464.

[52] Haonan Chen, V. Chandrasekar: High Resolution Rainfall Mapping in the Dallas-Fort Worth Urban Demonstration Network", *Proceedings of International Geoscience and Remote Sensing Symposium (IGARSS2012)*, Munich, Germany, July 22-27, 2012.

[53] B. E. Vieux and P.B. Bedient, 2004: Assessing urban hydrologic prediction accuracy through event reconstruction. *J. Hydrology,* 299, 217-236.

[54] W. F. Krajewski and A. J. Smith, 2002: Radar hydrology: rainfall estimation. *Advances in Water Resources*, 25, 1387-1394.

[55] V. Chandrasekar ; Haonan Chen and Masayuki Maki, 2012: Urban flash flood applications of high-resolution rainfall estimation by X-band dual-polarization radar network, *Proc. SPIE 8523, Remote Sensing of the Atmosphere, Clouds, and Precipitation IV, 85230K*, Tokyo, Japan.

[56] V. Koren, S. Reed, M. Smith, Z. Zhang and D. J. Seo, 2004: Hydrology Laboratory Research Modeling System (HL-RMS) of the U.S. National Weather Service,*J. Hydrol.*, 291, 297318.

[57] K. J. Westrick, C.F. Mass and B.A. Colle, 1999: The limitations of the WSR-88D radar network for quantitative precipitation measurement over the coastal western United States. *Bull. Amer. Meteor. Soc.*, 80, 2289-2298.

[58] Brian R. Nelson, D. J. Seo, and Dongsoo Kim, 2010: Multisensor precipitation reanalysis. *Journal of Hydrometeorology*, 11.3, 666-682.

[59] David Kitzmiller and Coauthors, 2011: Evolving Multisensor Precipitation Estimation Methods: Their Impacts on Flow Prediction Using a Distributed Hydrologic Model. *J. Hydrometeor*, 12, 1414-1431.

[60] Zhang, J., and Coauthors, 2011: National Mosaic and MultiSensor QPE (NMQ) System: Description, Results, and Future Plans. *Bull. Amer. Meteor. Soc.,* 92, 1321-1338.